UNIVERSIDAD DE CHILE
FACULTAD DE CIENCIAS FÍSICAS Y MATEMÁTICAS
DEPARTAMENTO DE ASTRONOMÍA

THE IMPACT OF LARGE SCALE STRUCTURE ON THE LY$\alpha$ EMISSION AND
ABSORPTION OF GALAXIES AT $2.2 \leq z \leq 2.8$

TESIS PARA OPTAR AL GRADO DE
MAGÍSTER EN CIENCIAS, MENCIÓN ASTRONOMÍA

VICTORIA PAZ PÉREZ GONZÁLEZ

PROFESOR GUÍA:
GUILLERMO BLANC MENDIBERRI

MIEMBROS DE LA COMISIÓN:
VALENTINO GONZÁLEZ CORVALÁN
ANDREW NEWMAN
WALTER MAX-MOERBECK ASTUDILLO
GWEN RUDIE

SANTIAGO DE CHILE
2022

## EL IMPACTO DE LA ESTRUCTURA A GRAN ESCALA EN LA EMISION Y ABSORCION DE LY$\alpha$ EN GALAXIAS A $2.2 \leq z \leq 2.8$

Los estudios de evolución de galaxias tienen como objetivo comprender cómo se forman y evolucionan las galaxias, a partir de las condiciones iniciales del universo primitivo. El paradigma moderno de formación y evolución de galaxias considera como un proceso fundamental el intercambio de masa, energía y metales, entre las galaxias, el medio circungaláctico (CGM) que las rodea y el medio intergaláctico (IGM), proceso conocido como ciclo bariónico. El ambiente en el que viven las galaxias juega un papel importante en este ciclo de evolución de las galaxias. En el universo local ($z \sim 1$), las propiedades de las galaxias están correlacionadas con la densidad local del ambiente (ej., A. Dressler 1980; Postman and Geller 1984; Kauffmann et al. 2004; Cooper et al. 2006; Muzzin et al. 2012; Hahn et al. 2015; Darvish, Mobasher, Sobral, et al. 2016). Sin embargo, en epocas anteriores ($z > 1{,}5$), las observaciones que prueban la relación entre las propiedades de las galaxias y el medio ambiente son mucho menos definitivas (ver revisión de Overzier 2016), convirtiéndose en un tema investigación actual en estudios de evolución de galaxias. (A. B. Newman et al. 2020)

En este trabajo, nuestro objetivo es estudiar las condiciones ambientales de las galaxias en el "mediodía cósmico" ($z \sim$ 2.2 - 2.8), y rastrear el impacto de la densidad local del ambiente sobre la emisión de Lyman alfa (Ly$\alpha$) y la absorción de Ly$\alpha$. Este estudio se realiza con datos preliminares de LATIS, cuyo acrónimo en inglés es Lyman Alpha Tomography IMACS Survey, (A. B. Newman et al. 2020). LATIS mide la densidad local en la que viven las galaxias, posibilitando el tipo de estudios que pretende realizar este trabajo.

Para los estudios de emisión, seleccionamos 1258 galaxias de LATIS. En esta sección hay dos objetivos principales: primero, comprender cómo las propiedades internas de las galaxias son diferentes en diferentes entornos. Siguiendo el método de Oyarzun et al. 2017, estimamos una distribución de Ancho Equivalente de Ly$\alpha$ (P(EW)), basado en la magnitud $M_{UV}$ y la pendiente UV ($\beta$), que se miden a partir de la fotometría disponible. Encontramos que no hay cambios significativos en el P(EW) estimado en diferentes condiciones ambientales. Lo que significa que la emisión observada, en nuestro rango de densidad local, no cambia debido a procesos internos en las galaxias. El segundo objetivo, es determinar cambios en las distribuciones Ly$\alpha$ EW entre grupos de galaxias con diferentes condiciones ambientales. Medimos directamente el EW en los espectros de galaxias y sus distribuciones, para grupos de galaxias con diferentes densidades locales. No encontramos cambios estadísticamente significativos en la distribución EW de Ly$\alpha$ en función de la densidad local. Para los estudios de absorción, usamos una muestra de 1771 galaxias. El objetivo es explorar si hay algún cambio en la absorción de Ly$\alpha$ entre grupos de galaxias con diferentes condiciones ambientales. Exploramos la absorción diferencial en los espectros de galaxias combinados. Encontramos una disminución significativa en la absorción de HI alrededor de las galaxias que viven en los entornos de menor densidad, lo que cuantificamos a través de un proceso de ajuste de perfil de Voigt diferencial. Esta tendencia se explorará con más detalle en el futuro.

## THE IMPACT OF LARGE SCALE STRUCTURE ON THE LY$\alpha$ EMISSION AND ABSORPTION OF GALAXIES AT $2.2 \leq$ z $\leq 2.8$

Galaxy evolution studies aim to understand how galaxies form and evolve from the initial conditions of the early universe. The modern paradigm of galaxy formation and evolution considers as a fundamental process the exchange of mass, energy, and metals between galaxies, their surrounding circumgalactic medium (CGM), and the intergalactic medium (IGM), a process known as the baryon cycle. The environment in which galaxies live play an important role in this cycle of galaxy evolution. In the "local universe", up to redshift z $\sim$ 1, galaxy properties are correlated with environment or local density (e.g., A. Dressler 1980; Postman and Geller 1984; Kauffmann et al. 2004; Cooper et al. 2006; Muzzin et al. 2012; Hahn et al. 2015; Darvish, Mobasher, Sobral, et al. 2016). However, at earlier epochs (z $>$ 1.5), observations that probe the relation between galaxy properties and the environment are much less definitive (see review by Overzier 2016), becoming a current topic of research on galaxy evolution studies. (A. B. Newman et al. 2020)

In this work, we aim to study the environmental conditions of galaxies at cosmic noon (z $\sim$ 2.2 - 2.8), and trace the impact of environment or local density over characteristic features on high redshift galaxy spectra: Lyman alpha (Ly$\alpha$) emission and Ly$\alpha$ absorption, studied in separate sections on this document. Both these studies are performed using early data from LATIS, the Lyman Alpha Tomography IMACS Survey (A. B. Newman et al. 2020). LATIS measures the local density in which said galaxies live, enabling the type of studies that this work aims to achieve. The survey is described in detail in Section 2.

For our emission studies, we select 1258 of the 2596 galaxies from LATIS sample. In this section there are two main objectives: First, to understand how internal properties of galaxies, that modulate the production and escape of Ly$\alpha$ emission, are different in different environments. To achieve this goal we estimate a Ly$\alpha$ Equivalent Width distribution (P(EW)) based on the measurement of $M_{UV}$ and UV slope ($\beta$) from available photometry, following Oyarzun et al. 2017 method. We find that there are not significant changes of the estimated P(EW) over different environmental conditions. Meaning that observed emission in our studied range of environment do not change due to internal processes in galaxies. The second objective is to determine changes in the Ly$\alpha$ EW distributions between groups of galaxies with different environmental conditions. We measure directly the EW in the galaxy spectra and create distributions for galaxy groups with different local densities. We find no statistically significant changes in the EW distribution of Ly$\alpha$ emission as a function of local density. For our absorption studies, we use a sample of 1771 galaxies. The main objective is to explore whether there is some change in Ly$\alpha$ absorption between groups of galaxies with different environmental conditions. We explore the differential absorption present in galaxy spectra. We find a significant decrease in HI absorption around galaxies living in the lowest density environments, which we quantify via a differential Voigt profile fitting process and their fitted parameters. This trend will be explored in more detail in the future.

*A través del Universo*
*La luz viaja con paciencia.*
*Solo un verso la existencia*
*Donde todo está inmerso.*
*Con la física converso*
*Y voy descifrando pistas*
*Fundamental es la vista*
*Y el abstracto entendimiento.*
*Se suma un descubrimiento*
*Ahora soy especialista*

# Agradecimientos

Agradezco la oportunidad de hacer ciencia y todo el aprendizaje que me trajo recorrer este camino. Agradezco a mi madre y a mi padre. Por ser origen, por creer en mí siempre. A mi hermano, por ser la persona que más amo y me ama en el mundo. Soy demasiado feliz de compartir una historia y un vínculo tan hermoso contigo.

Agradezco a la historia de las mujeres en la ciencia, quienes trabajaron por nuestro acceso equitativo a la educación universitaria, lo que me permite estar acá. Agradezco a mis profesoras del colegio por incentivarme a seguir una carrera científica. A mis compañeras feministas. Agradezco el año 2018, en el que nos manifestamos en contra del acoso en las universidades. Al club de lectura feminista de Beauchef, por enseñarme tanto. A las mujeres científicas que más me han inspirado en la vida: mis compañeras, amigas y cofundadoras de Cazadoras de Estrellas. Daniela, Pía, Natalie, Constanza, Paula, Elise, Antonia, Teresa(s), Francisca, Jennifer, Juanita y Magdalena. Gracias por estos cuatro años de trabajo autogestionado. Siento esperanza por las niñas del futuro gracias a todo lo que hemos hecho.

A mi familia escogida del Coro fcfm: Mariana, Sebastian, Ian, Diego, Pablo, Max y Cesar. Gracias por cada oncecita, y por recordarme que el amor está ahí, en el espacio seguro para sentir, reflexionar y sanar. Gracias por compartir sus vidas con la mía, y gracias por compartir en especial el canto. Les amo con todo mi ser.

Agradezco a mi profesor guía Guillermo Blanc, por su entusiasmo en el quehacer científico, mantenerme motivada, y su paciencia infinita con mi proceso de crecimiento académico y personal. También a Andrew Newman y Gwen Rudie, por ser excelentes co-guías y estar siempre disponibles para atender mis dudas. También a Valentino González, por acompañarme desde el principio en este postgrado, por estar presente en el periodo más difícil, y también en la transición a un nuevo proyecto de tesis en 2019. Me sentí comprendida y acompañada cuando más lo necesitaba. De verdad gracias, jamás olvidaré el profesionalismo y buen trato recibido de parte de todas estas excelentes personas.

Y gracias a todo lo que me ayudó a mantener el sentido de propósito en mi vida. A todas las personas que no alcancé a mencionar aquí. A los amores en todas sus formas. Al baile, a la poesía, a la música, las historias, los libros, al yoga, la meditación, las montañas, al bosque esclerófilo, los ríos, el mar, las ciudades, las voces, las ideas. Me encanta estar viva y usar mi cuerpo para experimentar e interactuar con este planeta, con todos sus seres y abstracciones.

# Table of content

# List of Tables

# List of Figures

x

# Chapter 1

# Introduction

Galaxy evolution studies aim to understand how galaxies form and evolve from the initial conditions of the early universe. This includes understanding how the properties of different types of galaxies change with time under the effects of different physical processes. The modern paradigm of galaxy formation and evolution considers as a fundamental process the exchange of mass, energy, and metals between galaxies, their surrounding circumgalactic medium (CGM), and the intergalactic medium (IGM), a process known as the baryon cycle.

Less than a few hundred million years after the Big Bang, gas in the early universe began to accrete onto dark matter halos and cool to the point of forming the first galaxies. For stars to actually form in galaxies, gas must be accreted into dark matter halos, and cool within the interstellar medium (ISM). While inflowing gas is being gravitationally drawn into galaxies, the gas that is cooling and settling onto the ISM is typically battling shock heating due to interaction with other gas already in the halo. Absorption line studies (e.g. C. C. Steidel, Erb, et al. 2010) show that galactic winds have been observed to blow gas away from the disks of galaxies and expand to at least the virial radius of their halos ($r_{vir}$). These outflows are generated by feedback from star-formation, being responsible for ejecting metals into the ISM, circumgalactic medium (CGM), and intergalactic medium (IGM). Also active galactic nuclei (AGN) driven winds can eject enriched ISM gas to the CGM and IGM. Outflowing ISM gas must deposit its heavy elements at large distances in order to achieve the observed abundance of metals that we see in the CGM (Werk et al. 2014, Tumlinson et al. 2011, C. C. Steidel, Erb, et al. 2010, Tripp and Song 2012, Chen et al. 2001). When gas gets ejected from the metal enriched ISM of a galaxy due to various forms of feedback it could be fully ejected out to the IGM via outflows, or could remain bound to the galaxy to eventually fall back onto it after cooling and mixing with gas in the CGM. This second scenario signifies that the gas will eventually be recycled and reaccreted back onto the host galaxy. In summary, the galaxy baryon cycle describes this whole process of the inflow and outflow of gas, its transformation into stars, its ejection from the galaxy through winds, and perhaps its eventual return to the ISM (Faucher-Giguère, Kereš, et al. 2011, Ford et al. 2014, Christensen et al. 2016, Muratov et al. 2016) for the refueling of star formation (Oppenheimer et al. 2010). This process has been repeating for billions of years to feed the baryon cycle and the growth of galaxies.

A key role is played by the CGM in galaxy evolution. The CGM is the extended interface

between the ISM of a galaxy and the surrounding IGM. This component represents a gas mass reservoir and a repository of the mechanical and radiative energy produced by stars. Therefore, the CGM is a source for a galaxy's star-forming fuel, the venue for galactic feedback and recycling, and perhaps the key regulator of the galactic gas supply. The CGM has a low density, so it can be almost uniquely traced by absorption line experiments towards background sources, typically quasars. The intervening CGM associated with a foreground galaxy leaves a characteristic spectral feature becoming a useful tool to study galaxy evolution.

The IGM and the environment in which galaxies live also play an important role in this cycle of galaxy evolution. As A. B. Newman et al. 2020 describes: It has been found that up to redshift $z \sim 1$ (in the "local universe") galaxy properties are correlated with environment or local density (e.g., A. Dressler 1980; Postman and Geller 1984; Kauffmann et al. 2004; Peng et al. 2010; Alan Dressler, Oemler, et al. 1997; Cooper et al. 2006; Patel et al. 2009; Muzzin et al. 2012; Hahn et al. 2015; Darvish, Mobasher, Sobral, et al. 2016), and this connection seems to be closest for properties related to a galaxy's star formation history (e.g., Bamford et al. 2009; Blanton and Moustakas 2009; Lemaux 2019; Pelliccia et al. 2019 Tomczak et al. 2019). However, at earlier epochs z > 1.5, observations that probe the relation between galaxy properties and the environment are much less definitive (see review by Overzier 2016), becoming a current topic of research on galaxy evolution studies.

Measuring the evolution of environmental trends through cosmic history is key to understanding their origins. To date we know that different processes cause enviromental effects in galaxies, which are a mixture of physical processes that are sensitive to local density or halo mass (e.g., ram pressure stripping, starvation, galaxy interactions) along with differences in assembly history (e.g., earlier collapse of halos within large-scale overdensities; A. B. Newman et al. 2020). The particular epoch at $z \sim 2 - 3$, typically referred to as "cosmic noon", is of special importance in the evolution of galaxies. In that epoch stars were forming inside of galaxies at a 30 times greater rate than it is seen around us today (Madau et al. 2014), as an all time high. In this thesis work, our main goal is to study the environmental conditions of galaxies at cosmic noon ($z \sim 2.2 - 2.8$), and trace the impact of environment or local density over characteristic features of high redshift galaxy spectra: Ly$\alpha$ emission and Ly$\alpha$ absorption, separately.

## 1.1   The Lyman Alpha Sprectral Feature

Ly$\alpha$ is a strong spectral line of hydrogen found in galaxy spectra, that is produced when neutral hydrogen electrons decay from the n = 2 orbital to the n = 1 orbital, emitting a photon with a wavelength of 1215.67 Å, know as a Lyman alpha photon, that places the emission line in the ultraviolet side of the spectrum at rest frame. Ly$\alpha$ emission is a widely used tool in the study of galaxy evolution, especially useful to study the high redshift universe, because for high $z$ galaxies the UV line is observable on the visible/optical range of wavelength.

Ly$\alpha$ photons have a resonant nature, they are absorbed and reemitted by neutral hydrogen (HI) inside galaxies many times before escaping (if they do). This occurs because HI has a very large effective cross section at Ly$\alpha$ wavelengths, so an emitted Ly$\alpha$ photon encounters a neutral hydrogen atom ($HI$) easily on its way out the galaxy. Ly$\alpha$ photons have the

exact energy that allows the HI electron to transition from n =1 to n=2 when absorbing the photon. Rapidly *HI* becomes unstable and the HI electron falls again from n=2 to n=1 reemiting a new Ly$\alpha$ photon that continues traveling through the galaxy with a very short mean free path. They can keep encountering HI atoms and being absorbed and reemitted many times until they reach the low density outskirt of galaxies from where they can escape and be observed. Alternatively, they can run into dust grains and be absorbed, because dust also has a very high cross-section to absorb UV photons. They can also escape if there is a large velocity offset (blue or red-shifted with respect to the gas).

Therefore, the resonant nature of Ly$\alpha$ photons makes them sensitive to the properties of neutral hydrogen in the ISM, CGM and IGM (e.g. C. C. Steidel, Bogosavljević, et al. 2011; Hagen et al. 2014; Chonis et al. 2013; Cantalupo et al. 2014). They are also sensitive to dusty environments, so only a fraction escape the ISM. Of those that escape, some scatter in the CGM and produce the observed extended halo of Ly$\alpha$ emission on galaxy images.

Some high redshift galaxies are classified based on their presence of Ly$\alpha$ emission or absorption. Lyman Alpha Emitters (LAE) are high redshift galaxies characterized by the presence of a strong Ly$\alpha$ line at 1215 Å in their restframe, which makes them easily observable by optical telescopes (due to the redshift produced by the expanding universe). On the other hand, Lyman Break Galaxies (LBG) are characterized by a "dropout" or "break" on their spectra at wavelenghts shorter than 912 Å , known as the Lyman limit. This is produced because radiation at higher energies than the Lyman limit is almost completely absorbed by neutral gas around star-forming regions and in the CGM and IGM. For high redshift galaxies the Lyman break will appear to be at optical wavelengths making them, as LAEs, easy to identify with optical telescopes.

### 1.1.1   Lyman Alpha Emission Studies

When studiying Ly$\alpha$ Emission of galaxies, estimations of its escape probability, its line shape or its Equivalent Witdh (EW) are measured and related to physical processes inside and around galaxies. The EW is a measurement of the line flux intensity relative to the continuum flux, in this work EW will be our main tool to study Ly$\alpha$ emission, as seen in following Sections.

Oyarzun et al. 2016, Oyarzun et al. 2017 solidly establishes how the Ly$\alpha$ EW distribution and Ly$\alpha$ photon escape probability depend on the stellar mass, UV-luminosity, and UV-slope (a proxy for dust content) of high-$z$ galaxies. They find that these trends have an important impact on the interpretation of epoch of reionization results based on the measurement of the fraction of high EW systems as a function of redshift, as galaxy properties also evolve. While the dependence of Ly$\alpha$ emission on galaxy properties is now well established, almost no observational constraints are available on how it depends on the large scale environment in which galaxies live. It is expected that environmental effects on the Ly$\alpha$ EW distribution and escape fraction exist, both due to the direct impact of the local IGM structure and kinematics on Ly$\alpha$ radiative transfer (Ly$\alpha$ RT), and due to correlations between environment and galaxy properties affecting the production and escape of Ly$\alpha$ photons.

The escape probability of Ly$\alpha$ photons from galaxies has been used to trace the build up
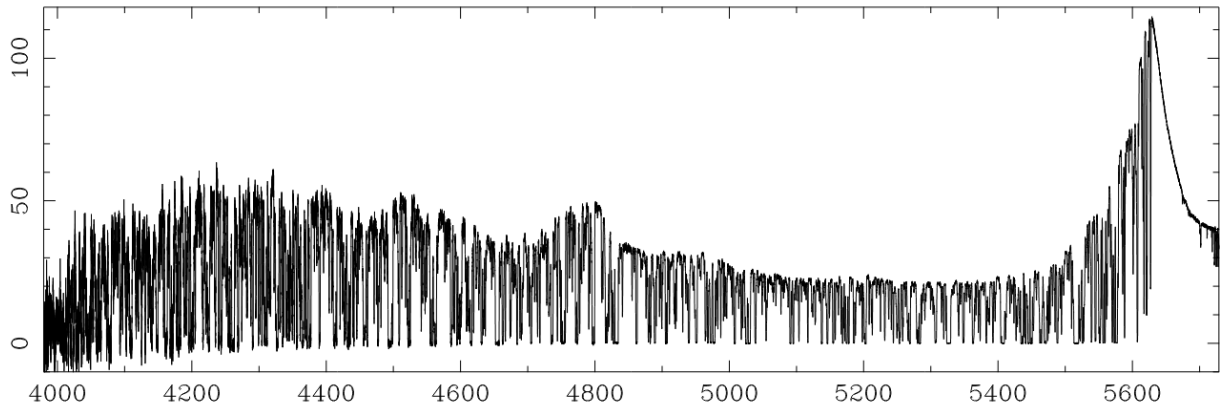
Figure 1.1: Example of high resolution spectrum of a QSO at redshift 3.63, taken with the HIRES spectrograph in the Keck 10 m telescope in Hawaii. The plot shows the flux of the QSO in arbitrary units versus the observed wavelength in units of Å. The noise level can be judged from the longer wavelength wing of the broad, intrinsic Lyα emission line of the QSO (near 5650 Å). All of the ragged features are high redshift absorption lines. Most of the lines between the QSO's Lyα and Lyβ emission lines (the humps at 5650 and 4750 Å) are due to Lyα absorption by intervening gas, creating the Lyman Alpha Forest where the emission lines are the "trees". The actual rate of incidence of absorbers decreases towards shorter wavelengths (lower redshifts). Nevertheless, the line density increases to the blue because higher order absorption lines from the Lyman series appear and overlap randomly with Lyα lines of systems at lower redshifts . Image from Murdin 2000

of dust in the ISM throughout cosmic history (Hayes et al. 2011; Blanc et al. 2011), and to characterize the last stages of the re-ionization epoch by measuring changes in the Lyα EW distribution and the clustering of Lyα Emitters (LAEs) as a function of redshift (e.g. D. P. Stark et al. 2010; Treu et al. 2013; Momose et al. 2014; Ouchi et al. 2018). Furthermore, Lyα is currently being used to study cosmology and the evolution of dark energy out to $z \sim 3$ by measuring the large scale clustering power spectrum of LAEs at high redshift (Adams et al. 2011; Hill, Gebhardt, et al. 2008; Hill and HETDEX Consortium 2016). Moreover, the escape probability of Lyα photons from the ISM and CGM of galaxies has been observed to depend on the properties of galaxies. This dependence is expected as the radiative transfer of Lyα is highly sensitive to the presence of dust, the column density and geometric structure of HI, and the overall kinematics of the gas in which Lyα photons scatter as they propagate out of the galaxy. All these characteristics are related to the stellar mass, metallicity, gas fraction, and the star formation and associated galactic outflow activity of galaxies.

The structure and kinematics of HI gas in the CGM and IGM directly affects observable properties of Lyα line emission. Examples of these properties include the observed Lyα spectral line shape (e.g., Gronke et al. 2016,Gronke et al. 2017), and the surface brightness profiles of extended Lyα halos around galaxies (e.g. Cantalupo et al. 2014;J. F. Hennawi et al. 2015). A proper understanding of circumgalactic and intergalactic Lyα radiative transfer (RT) would allow us to use observations of the Lyα emission as a tool to study the circum-/inter galactic gaseous environment.

4

### 1.1.2   Lyman Alpha Absorption Studies

The most characteristic absorpion feature at rest-frame UV wavelengths of high redshift galaxies and QSOs is the Lyman Alpha forest (see Figure 1.1). The Lyman alpha forest is a series of Ly$\alpha$ absorption lines typically seen in the spectra of high-z QSOs and galaxies, between the Lyman Limit (912 Å) and the wavelength of Ly$\alpha$ (1215 Å). These absorption lines are produced by intervening clouds of neutral hydrogen at lower redshifts, along the line of sight towards the background object. It is a direct observational evidence of the existence of the IGM.

Early models of Ly$\alpha$ absorption systems predicted the absorption lines as arising from discrete 'clouds' of gas in intergalactic space. Since neutral hydrogen clouds at different positions along this line-of-sight see the photons at different wavelengths (due to the redshift), each individual cloud leaves its fingerprint as an absorption line at a different position in the observed spectrum blueward of Ly$\alpha$ with respect to the galaxy.

It is worth keeping in mind that, even the term 'cloud' does already imply a prejudice as to the spatial distribution of the gas. Before the advent of cosmologies dominated by dark matter (which supplies the gravitational attraction necessary to hold together the gas), it was thought more likely that the intergalactic clouds would be confined by the pressure of an even hotter and more tenuous intercloud medium. In this model, a cloud would be homogeneous, static or slowly expanding and, at least for some of its lifetime, in thermal photoionization equilibrium with the UV background. Such an object has a simple observational signature in absorption.

With only the intrinsic atomic line width of the Ly$\alpha$ transition and purely thermal motions contributing to the absorption line broadening, the result is a so-called Voigt profile. The decomposition into Voigt profiles had originally been justified by the assumption that Ly$\alpha$ absorption systems are discrete, pressure-confined gas clouds in hydro-static, thermal and ionization equilibrium, floating in intergalactic space. This picture provided an analytically tractable model which made a host of testable predictions, several of which unfortunately contradicted the observational evidence. This simple model of 'clouds' conforming the IGM was finally discarded, as strong evidence kept piling up, such structure formation cosmologies dominated by the presence of large amounts of dark matter. The gravitational collapse of dark matter would have trapped large amounts of baryonic gas as well. The cold dark matter (CDM) structure formation scenario predicts a large abundance of collapsed CDM halos with individual masses too small to form stars and turn into galaxies. Warm photoionized intergalactic gas sinks into these 'mini'-halos or accretes onto dark matter filaments and sheets. These structures are visible only in absorption since there are no stars which could produce any light. A breakthrough in cosmology occurred in the early 1990s when hydrodynamic cosmological simulations became available. If the underlying cosmological picture (a universe dominated by cold dark matter) is correct, then the hydro-simulations are telling us that the spatial distribution and physical state of the Ly$\alpha$ forest gas is more complex than previously thought. The gas is arranged in filaments and sheets, in what has been called the 'cosmic web', closely tracing the dark matter distribution on large scale. (Murdin 2000).

## 1.2 Lyman Alpha Tomography

As stated before, in this thesis our main goal is to study the environmental conditions of galaxies at cosmic noon ($z \sim 2.2 - 2.8$), and trace the impact of environment or local density over Ly$\alpha$ emission and Lyman alpha absorption. As A. B. Newman et al. 2020 describe, is very difficult to conduct environmental studies at higher redhshifts. To quantify galaxy environment and to map large-scale structures present diverse impediments. For example, massive overdensities at $z > 2$ are diffuse, with a modest density contrast spread over tens of arcmin scales (Chiang et al. 2013). Although galaxy density can be used as an indicator of environment, spectroscopic surveys at these redshifts cover smaller volumes with poorer sampling than at z = 1. Furthermore, increasing photometric redshift errors degrade environmental measures beyond z $\sim$ 1.2 (Darvish, Mobasher, Martin, et al. 2017). Finally observations of an intragroup or intracluster medium push the sensitivity limits of present X-ray and CMB observatories and will miss massive structures at z $>$ 2 that have not yet developed a hot atmosphere.

One of the best developed techniques to measure galaxy environments and detecting large-scale structures at high redshift (z $\sim$ 2 − 3) is called IGM or Ly$\alpha$ Tomography. With this technique it is possible to map the opacity of the intergalactic medium (IGM). The physical principle behind it, is that the Ly$\alpha$ forest in galaxy spectra arises from trace amounts of $HI$ in photoionized gas that is around galaxies. On scales larger than roughly the Jeans length ($\sim$ 100 comoving kpc; Gnedin and Hui 1998; Kulkarni et al. 2015), the distribution of $HI$ follows that of the dark matter. Using the Ly$\alpha$ forest observed in quasars the structure formation can be studied. (see reviews by Rauch 1998;McQuinn 2016). Quasar observations probe the matter distribution only along a single sightline. Ly$\alpha$ Forest Tomography consist in observing a bundle of sightlines piercing the same volume. The three-dimensional (3D) matter distribution can be reconstructed from those observations (Pichon et al. 2001; Caucci et al. 2008).

Using Ly$\alpha$ Forest Tomography, tomography surveys can be made. These surveys are these 3D matter density distribution reconstructions made from several QSOs and galaxy spectra piercing a volume. These surveys enable us to study both the galaxies surrounding, such as CGM and IGM, from the Ly$\alpha$ absorption in the background galaxy and QSO spectra (at z $\sim$ 2−3, see Adelberger, C. C. Steidel, et al. 2003,Adelberger, Shapley, et al. 2005; Jeff Cooke et al. 2006; Crighton et al. 2011; Rakic et al. 2012; Rudie, C. C. Steidel, Trainor, et al. 2012; Lee, J. Hennawi, et al. 2014; Tummuangpak et al. 2014; Turner et al. 2014) and also tu study the ISM properties of galaxies from direct spectroscopy. See figure 1.2 from Kakiichi, Majumdar, et al. 2017 for a scheme of how these tomographic surveys work.

The technical requirements to perform this reconstructions are very high, because it requires spectroscopy of very faint sources with moderate spectral resolution and relatively high signal-to-noise ratios, which must await 30m-class telescopes. The resolution achievable in such a reconstruction depends on the density of sightlines that are observed. With a sufficiently high density, multiple sightlines will probe the distribution and kinematics of $HI$ and metals in the circumgalactic gas surrounding individual galaxies (scales of $\sim$ 300 kpc), enabling the flow of gas between galaxies and their gaseous halos to be studied in unprecedented detail (Theuns and Srianand 2006;C. Steidel et al. 2009; Evans et al. 2012;
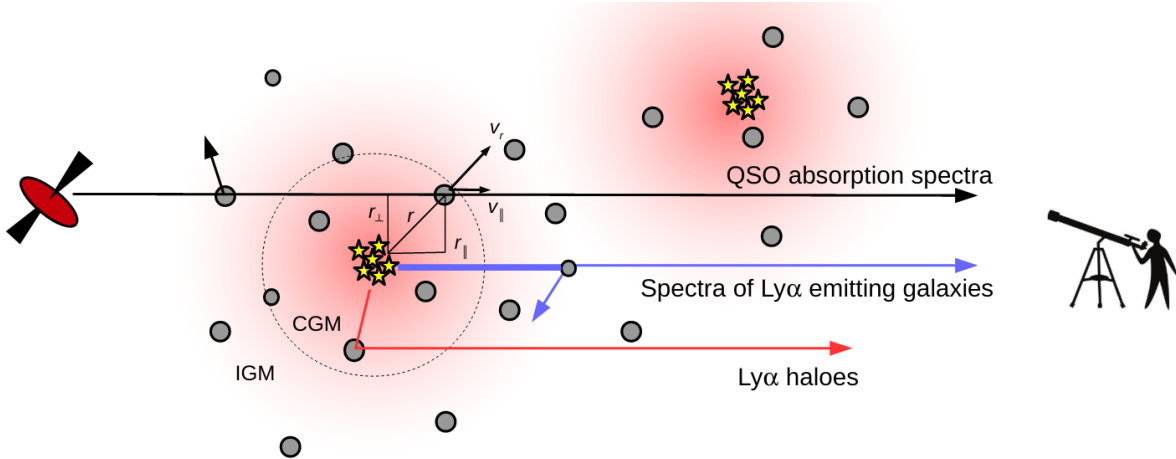
Figure 1.2: Schematic illustration of a spectroscopic survey of Lyα emitting galaxies in QSO fields. Galaxies (represented as a collection of star symbols) reside in gaseous environments composed of the neutral gas (represented by grey-coloured clumps). The dashed circle indicates the viral radius of host dark matter halo. Some Lyα photons emitted from the galaxies are scattered back to observers, contributing to the Lyα haloes (represented by fuzzy red spheres). The cartoon illustrates how we observe (i) QSO absorption spectra, (ii) spectra of Lyα emitting galaxies, and (iii) Lyα haloes around galaxies trace the circum- and intergalactic gas and their interconnections. Image from Kakiichi and Dijkstra 2018

A. Newman et al. 2019; Rudie, C. C. Steidel, Pettini, et al. 2019).

There is a way to reduce the observational requirements, if the goal is changed to just map the IGM with a resolution of a few comoving Mpc (cMpc). As A. B. Newman et al. 2020 say, on these larger scales of $\geq 3h^{-1}$ cMpc, the mean Lyα opacity is expected to be well-correlated with the matter density (McDonald et al. 2002; Kollmeier et al. 2003; Cai et al. 2016) and is observed to correlate with the galaxy density (Adelberger, C. C. Steidel, et al. 2003). Measuring this does not require identifying individual Lyα absorption lines, only spatially coherent flux decrements within the Lyα forest, which can be measured in fairly noisy spectra. In this way this technique becomes practical with current facilities.

IGM Tomography has been proved to be effective through mock surveys (C. W. Stark et al. 2015) and also observational implementations (Lee, J. Hennawi, et al. 2014). The COSMOS Lyman-Alpha Mapping and Tomography Observations (CLAMATO) survey, was the first observational implementation of this technique. The CLAMATO map now covers an area of 0.16 deg$^2$ spanning z = 2.05-2.55 with a resolution set by $< d_{\perp} > = 2.5h^{-1}$ cMpc (Lee, Krolewski, et al. 2018). As A. B. Newman et al. 2020 say, this map has demonstrated the power of Lyα tomography via several applications, including a study of a protocluster at z = 2.44 with a tomographic mass of $(1.1 \pm 0.6) \times 10^{14} h^{-1}$ M (Lee, J. F. Hennawi, et al. 2016) and the identification of a sample of voids (Krolewski et al. 2018).

A. B. Newman et al. 2020 present preliminary results of the Lyman Alpha Tomography IMACS Survey (LATIS), a newer and larger tomographic map than CLAMATO that (when complete) will cover an area of 1.7 deg$^2$ and a volume of $10^7$ cMpc$^3$ with $\sim 1$ pMpc resolution.

LATIS is large enough to contain a representative sample of structures from protoclusters to large voids. The survey is described in detail in Section 2.1.

## 1.3    This work

On this thesis we present a study of the impact of large scale structure on the Ly$\alpha$ emission and absorption of high redshift galaxies (z $\sim 2.2 - 2.8$). Preliminary results from LATIS are used, LATIS is a spectroscopic survey conducted with the Magellan 6.5m telescope, designed to map the $z = 2.2 - 2.8$ IGM in three dimensions by observing the Ly$\alpha$ forest in the spectra of galaxies and QSOs (A. B. Newman et al. 2020). We perform separate Ly$\alpha$ emission and absorption studies using a preliminary sample of $\sim$ 2900 galaxies from the LATIS survey. We also use the environmental density ($\delta f$) derived in A. B. Newman et al. 2020 from the tomographic reconstruction of the LATIS survey spectra, to study how the Ly$\alpha$ emission and absorption properties of galaxies depend on environment. LATIS is introduced and described in detail in Chapter 2.

In order to study the effect of environment on Ly$\alpha$ emission it is necessary to take into account how this emission is affected by the internal properties (e.g. luminosity, dust content) of the galaxies that populate different environments. Oyarzun et al. 2017 determined how Ly$\alpha$ EW and escape probabilities depend on the galaxy properties mentioned above, creating a probability of equivalent width distribution of Ly$\alpha$ model P(EW) as a function of UV Magnitude ($M_{UV}$) and UV slope ($\beta$). Chapter 3 explains how we first obtain UV luminosity and $\beta$ from LATIS galaxy spectra, then use them to estimate P(EW) with the model proposed by Oyarzun et al. 2017, to finally estimate the baseline level of variation we expect to see in the Ly$\alpha$ EW distribution between the different enviornmental density bins in our sample, simply due to changes in galaxy internal properties. Obtaining the P(EW) for each group and determining how it changes due to galaxy properties on each density bin. Once that is established, on Chapter 4 we go further and measure directly EW distributions of galaxies in different environments and see how they change due to local density. On Chapter 5 we search for variations in the Ly$\alpha$ absorption profile of galaxies as a function of environment. We find a significant decrease in HI absorption around galaxies living the lowest density environments, which we quantify via a differential Voigt profile fitting process. Finally we conclude and summarize our main results in Chapter 6.

# Chapter 2

# Data: LATIS and Tomographic Density

## 2.1 The Lyman Alpha Tomography IMACS Survey

LATIS (A. B. Newman et al. 2020) is a tomographic survey conducted using the Inamori-Magellan Areal Camera and Spectrograph (IMACS; Alan Dressler, Bigelow, et al. 2011) at the Magellan Baade telescope. LATIS performs Ly$\alpha$ tomography by densely sampling the Ly$\alpha$ forest in a network of Lyman-break galaxies (LBG) and QSOs with an average transverse separation of $2.5h^{-1}$ comoving $Mpc$ (1 physical Mpc = 1 cMpc). The goal of LATIS is to map a representative volume of the distant universe ($z = 2.2$–$2.8$). When complete, LATIS will cover 1.7 deg$^2$, corresponding to a volume of $4 \times 10^6$ h$^{-3}$ cMpc$^3$. The observed fields correspond to three of the Canada–France–Hawaii Telescope Legacy Survey (CFHTLS) deep fields (called D1, D2/COSMOS, and D4): Half of the LATIS area covers the D2/COSMOS field and the other half is divided between D1 and D4. These four observed fields are divided into "footprints", depending on the area covered by the instrument IMACS field-of-view. The four fields are divided into 12 footprints as shown in figure 2.1. This survey observes high-z galaxies and QSOs. All the observed galaxy spectra are Lyman break galaxies (LBG), *ugr* color selected, and for COSMOS field galaxies the selection was supplemented with photometric redshifts, (more detail into galaxy spectra in Section 2.2).

The reason why these type of galaxies are selected for creating the survey are described in detail in LATIS paper A. B. Newman et al. 2020. As is explained there, basically the sample selection was determined by two goals: first, to achieve the highest practical signal-to-noise ratio in the tomographic map, and second, to mantain a well-defined selection function so that the properties of galaxies in different environments can be robustly characterized. So the selection was made by a relative simple and inclusive color criteria, suplemented by public databases of spectroscopic redshifts for a minority of targets (See A. B. Newman et al. 2020).

The parameters that drove the main survey design decisions are:

- *Area*: 1.7 de$g^2$ , wide enoguh to identify a statistical sample of structures (20 proto-clusters).
- *Survey fields*: CFHTLS fields were selected for their deep, homomgeneus optical imaging over the necessary area, their good visibility from Las Campanas Observatory
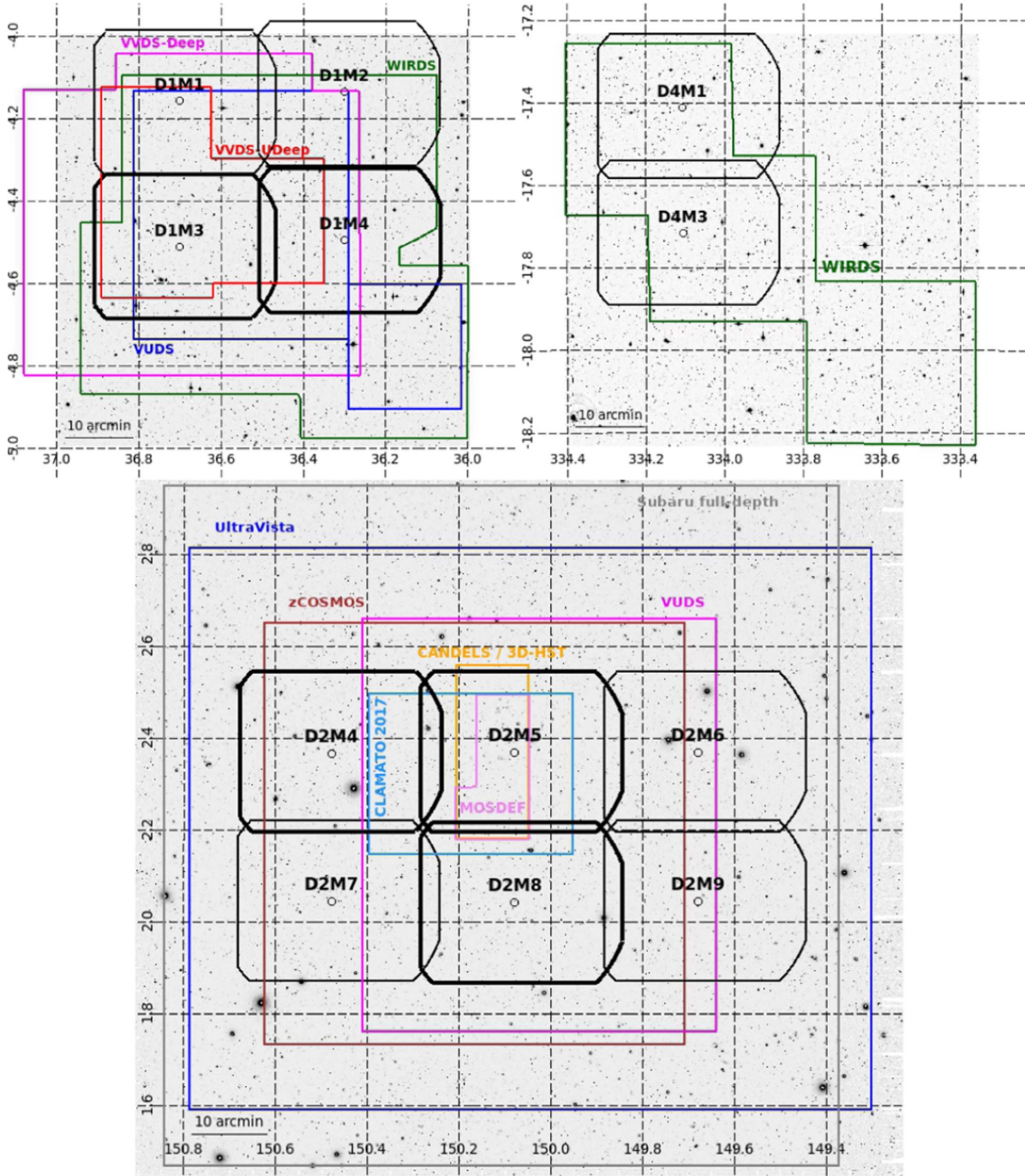
Figure 2.1: This Figure is from the paper A. B. Newman et al. 2020, Figure 1: *The planned positions of the 12 IMACS footprints that comprise LATIS (black outlines) are overlaid on r-band images of each field and labeled. Thicker black outlines show the five footprints containing the observation used in this work. The top-left and right panels show the CFHTLS D1 and D4 fields, respectively, and the bottom panel shows D2/COSMOS. The footprints of various other surveys are overlaid for reference. Axes show the R.A. and decl. in degrees.*

(LCO) and also because they are well-observed and benefit from a legacy of deep imaging and spectroscopy.

- *Instrument*: IMACS was selected as the ideal instrument for LATIS due to the wide field-of-view of 0.5 deg of its f/2 camera. A custom grism and filter with a passband of 383-591 nm were made specially to carry out these observations, providing an average spectral resolution of R=880 in the Ly$\alpha$ forest. The wavelength range is defined by the drop in the instrument throughput on the blue, and the desire to observe CIV absoption on the red. In this setup we can observe targets over 0.15 deg$^2$ with full spectral coverage over this bandpass. IMACS is among the most efficient instruments worldwide for conducting LATIS due to its mapping speed compared with others.

- *Target density*: With the adopted IMACS configuration, 3600 targets per deg$^2$ are observed in the LATIS survey. About half of them are ultimately useful for tomographic mapping providing a total sightline density of 1800 targets de$g^2$. However, an individual sightline does not only probe the redshift range of the reconstruction. A single sightline spans $\Delta z \sim 0.3$ on average, translating into a mean sightline density of $\sim 900$ deg$^{-2}$ at any given redshift inside the $2.2 < z < 2.8$ range of the tomographic maps.

Observations of LATIS were performed between 2019 and 2021 at Las Campanas Observatory (LCO), specifically at the Baade Magellan Telescope. As a master student I had the opportunity of participating in 5 observing runs during 2019, and learn how to operate the instruments for the observations at the telescope.

Along with spectroscopic observations obtained with IMACS for the LATIS project, in this work we make use of available broad-band photometric catalogs for galaxies in the LATIS fields. In the D1 and D4 fields, the basis for the photometric catalogs is the final release (T0007) of the CFHTLS. In the D2/COSMOS field, the Ilbert et al. 2009 catalog of I < 25 sources covering 2 deg$^2$ with 30-band photometry is used.

At the time of writing, LATIS observations are complete, but early data discussed in the LATIS paper (A. B. Newman et al. 2020) is reported to be processed and vetted over one-third of the survey area, corresponding to 0.58 deg$^2$ covered over 4 out of the 12 footprints: 3 footprints in COSMOS (D2M4, D2M5, D2M8) and 1 footprint in the D1 field. Complete observed footprints are marked in bold squares in figure 2.1 (A. B. Newman et al. 2020). Over these areas the observations cover 2895 galaxies.

In this work we use this preliminary LATIS sub-sample to carry out our intended studies of Ly$\alpha$ emission and absorption over the $\sim 2895$ galaxy spectra that LATIS provides between redshifts $z = 2.2 - 2.8$. Along with the galaxy spectra, LATIS provides estimations of local density from tomographic maps that give us $\delta f$ values within the studied volume, $\delta f$ is a measure for density of environment, or local density. For more details on how this value is obtained see section 2.3

## 2.2 Characterization of LATIS galaxy spectra

LATIS galaxies are Lyman Break Galaxies (LBG), observed between a wavelength range of $4000 - 5750$ and they are as faint as $g \sim 24.5$ mag. The observed redshift ($z$) range of these galaxies are between $2.2 - 3.2$ giving us a restframe wavelenght range between

| Type | Observed to Date | Full LATIS |
|---|---|---|
| All targets | 2596 | 6929 |
| $z = 2.2 - 3.2$ galaxies/QSOs | 1593 | 4250 |
| with `zqual` $\geqslant 3$ | 1425 | 3800 |
| Used for tomography | 1071 | 3210 |

Table 2.1: This Table is from the LATIS paper (A. B. Newman et al. 2020), Table 1: It shows the inventory of main Target sets. *The right column shows extrapolations to the full LATIS survey. Each row is a subset of the last.*

$\sim 1050 - \sim 1800$ enough to include Ly$\alpha$ Forest and Ly$\alpha$ emission on their observed spectra. The redshifts for the galaxies in the sample are determined by LBG spectral modeling, as they describe in the paper in section 7 (A. B. Newman et al. 2020). LATIS paper also describes a *redshift quality flag*: *zqual*. It is determined by inspecting one by one every target through an interactive GUI, where they try to identify the spectrum and measure an approximate initial redshift, using reference composite spectra and SDSS templates (from Shapley et al. 2003). *zqual* goes from 0 to 4 in the LATIS catalog, where 0 corresponds to the targets where no redshift could be assigned to the spectrum, 1 corresponds to spectra where a single emission was identified and assumed to be Ly$\alpha$, 2 corresponds to low-confidence guess redshift, 3 corresponds to high-confidence redshift, determined by multiple observed lines and a well-modeled spectrum, and finally 4 corresponds to targets with a certain redshift value, high signal-to-noise spectrum, with numerous lines identified.

To date 2596 galaxies have been processed and vetted by LATIS, these galaxies are used for tomographic reconstruction, thus they have to meet the following conditions: to be in the expected redshift range between $2.2 - 3.2$, to have high quality redshifts (`zqual` $\geqslant 3$), and meet enough sightline separation within tomographic area for reconstruction. In most fields the average separation between sightlines is relatively constant at $< d_\perp > \sim 2.5h^{-1}$cMpc over $z = 2.2 - 2.6$, meeting the design goal of the survey mentioned in Chapter 2.1. At $z > 2.6$ the sigthline density declines, and at $z < 2.8$ it falls down to $< d_\perp > = 4$ h$^{-1}$ cMpc, which is the maximun useful value based on simulations by C. W. Stark et al. 2015. Therefore from 2596 available galaxy spectra A. B. Newman et al. 2020 end up with a final selection of 1071 sightlines for tomographic reconstruction as seen in Table 2.1. (A. B. Newman et al. 2020).

## 2.3   Tomographic Local Density Definition $\delta f$

In this work we intend to perform environmental studies over Ly$\alpha$ emission and absorption of LBG galaxies at high redshift. LATIS provides a measure for the environment where these galaxies live: the flux contrast $\delta f$. $\delta f$ is a measure for density of environment or local density measured directly from the 1071 galaxy spectra described above, reconstructing the transmitted flux F through the Ly$\alpha$ forest. (Pichon et al. 2001; Gallerani et al. 2011; Horowitz et al. 2019; A. B. Newman et al. 2020).

$\delta f$ is defined as the fractional variation with respect to the mean transmitted flux of the spectra over redshift:

$$\delta f = \frac{F}{<F(z)>} - 1 \qquad (2.1)$$

where F is the fraction of the flux of a galaxy spectrum that is transmitted through the Ly$\alpha$ forest at any given redshift. It is measured directly from the continuum normalized galaxy spectrum over the Ly$\alpha$ forest region. $<F(z)>$ is the mean transmission of the Ly$\alpha$ forest of galaxies at redshift $z$ (Faucher-Giguère, Prochaska, et al. 2008). Both values can be obtained directly from the galaxy spectra mentioned in previous section.

When the $\delta f$ value is lower or more negative, we have lower transmitted flux and hence higher HI density, and vice versa, when the value of $\delta f$ is higher or more positive, then we have more transmitted flux and therefore, a lower local density measure.

## 2.4 Tomographic map reconstruction

The method used for the reconstruction of tomographic maps is Wiener filtering, a widely used method in the mapping of large-scale structure. The Wiener filter incorporates noise weighting and regularizes the output map, as described below, this method was investigated theoretically by Pichon et al. 2001 and Caucci et al. 2008, and more recently by C. W. Stark et al. 2015 in the context of the CLAMATO project, mentioned in the introduction. For LATIS the `dachshund` code developed by C. W. Stark et al. 2015 is used (A. B. Newman et al. 2020).

LATIS A. B. Newman et al. 2020 describes, that with this method a volume can be reconstructed considering, for each galaxy, the $\delta_f$ and their associated uncertainties $\sigma_\delta$ at a series of position $(x, y, z)$ within the volume. The coordinates $(x, y, z)$ are expressed in $h^{-1}$ cMpc and are aligned with the R.A., Dec., and redshifts axes respectively. Each such measurement is one pixel in the Ly$\alpha$ forest of a background source. These sky coordinates and redshifts are converted into $(x, y, z)$ coordinates using redshift-dependet radial and transverse comoving distances.

Although the line-of-sigth coordinate is expressed as a distance, the map does not correct for peculiar velocities, so the map is made in velocity space. (A. B. Newman et al. 2020)

Finally, (A. B. Newman et al. 2020) reports that the IGM opacity is reconstructed by 173185 data points in two volumes: D2/COSMOS and D1 fields, with dimensions $64 \times 51 \times 483 h^{-3} cMpc^3$ and $33 \times 27 \times 483 h^{-3} cMpc^3$ respectively. Figure 2.2 show their distribution, also notice that one quadrant of COSMOS volumes has no sightines yet, that region is excluded, leaving a total volume of $1.7 \times 10^6 h^{-3} cMpc^3$ in the maps. Each "voxel" occupies $(1 h^{-1} cMpc)^3$. Wiener filtering interpolates between the sightlines to estimate $\delta_f$ in each voxel. For most applications, the Wiener-filtered maps are then smoothed using an isotropic Gaussian kernel, this reduces the noise at the expense of resolution. On this work $\sigma_{kern} = 2 h^{-1} cMpc$ is used. See reconstructed maps in Figure 2.3
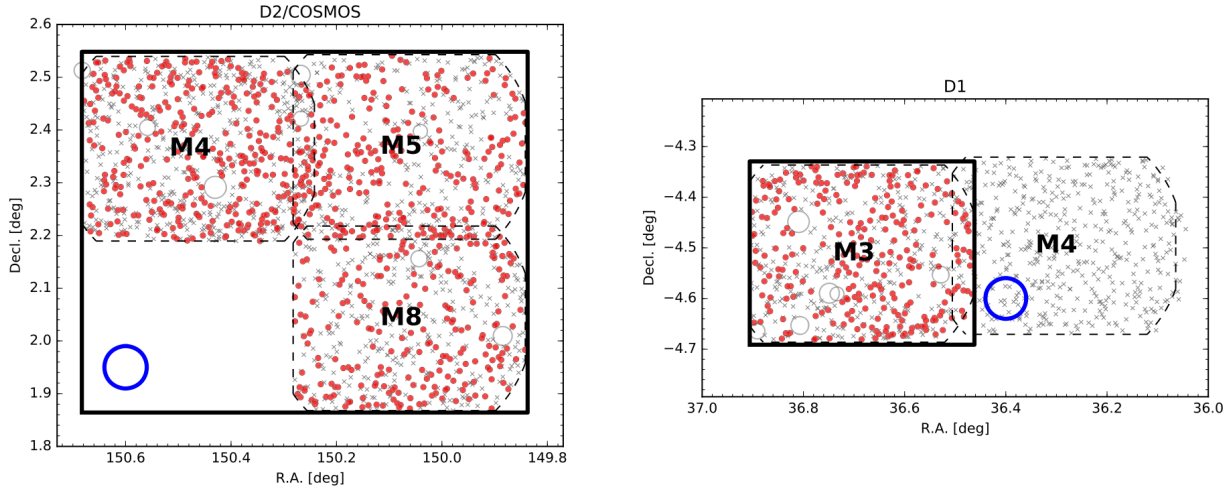
Figure 2.2: This Figure and Caption are from LATIS paper, A. B. Newman et al. 2020, Figure 2.2: *The positions of targeted galaxies in the COSMOS (left panel) and D1 (right) fields. Red circles represent targets used for Lyα forest measurements, while gray crosses indicate targets that were not used to construct LATIS maps (usually foreground galaxies). Dashed lines outline the individual IMACS footprints. The D1M4 field is not used for tomography in this study because the processing of both target sets is not yet complete. Thick black lines indicate the border of the tomographic maps Blue cicles have a radius of $3h^{-1}$ cMpc and so approximate the tomographic map resolution element. Light gray circles enclose the largest regions (radius > 45") from which targets are excluded, due to a bright star.*
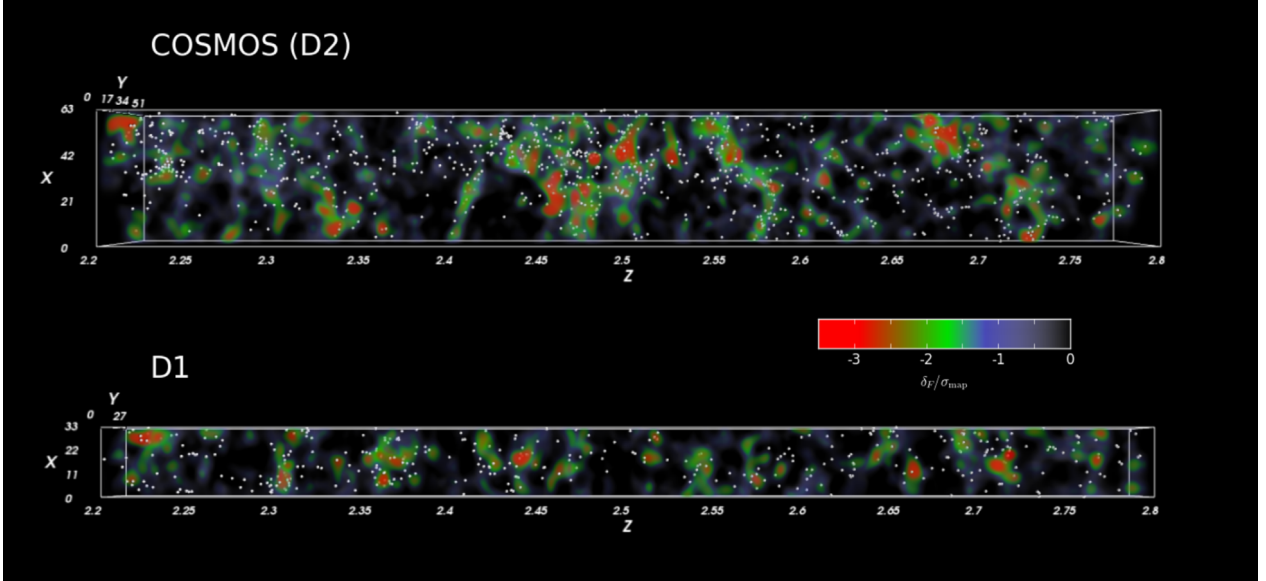
Figure 2.3: This Figure and Caption are from LATIS paper, A. B. Newman et al. 2020, Figure 2.3: *Renderings of the IGM opacity in the LATIS fields observed to date. The COSMOS (top) and D1 (bottom) maps, smoothed by $\sigma_{kern} = 2h^{-1}cMpc$, are each viewed in asie-on projection. The z-axis shows the redshift while the $x-$ and $y-$axes are in $h^{-1}cMpc$. Red colors correspond to more negative $\delta_F$, i.e., lower transmitted flux and higher matter densities, while bluer colores represent the reverse. Regions with $\delta_F > 0$, i.e., with higher than mean transmission, are completely transparent in these renderings. The positions of galaxies from LATIS, VUDS and zCOSMOS surveys are overlaid. Note that one quadrant of the COSMOS volume is not yet observed,* see figure 2.2.

# Chapter 3

# Dependence of the Ly$\alpha$ Emission on Galaxy Properties

This work intends to perform environmental studies of Ly$\alpha$ emission of high-z galaxies using LATIS preliminary data. The main problem with environmental studies is that if a trend over environment is found it could be interpreted as something directly related to environment or it can come from the fact that different galaxy populations are found in different environments, affecting the observed feature.

For example, different environments produce different halo distributions in galaxies, which affects their masses, that are related to how much star formation (SF) and dust we find inside them. In particular for Ly$\alpha$ emission, its observed shape can be affected by different factors such as its production inside galaxies but also by its escape and propagation through the CGM and IGM.

These may be small differences but if the goal is to isolate the direct impact of environment, then first it is necessary to understand how internal properties of galaxies, related to the production and escape of Ly$\alpha$ photons, are different in different environments. It is necessary then to identify how Ly$\alpha$ emission is affected by these internal processes over a range of local density values, and measure it. Any difference that might be found in Ly$\alpha$ due to these internal processes can be considered and compared later in environmental dependence studies, over the same range of density values (such as that in Section 4). Finally, if after considering internal processes effects environmental trends are still found, they can be interpreted as actual propagation in the CGM and IGM.

In this section we study how galaxy properties such as UV-luminosity ($M_{UV}$) and UV-slope ($\beta$, a proxy for dust content) change as a function of environment in our sample. We estimate the level of variation we expect in the Ly$\alpha$ Equivalent Width (EW) distribution due to these changes. We want to test if the changes that could arise in Ly$\alpha$ EW distribution are due to changes in the properties of the galaxies that live in different environments.

Oyarzun et al. 2017 determine how Ly$\alpha$ Equivalent Width (EW) distribution depends on galaxy properties such stellar mass ($M_*$), UV-luminosity ($M_{UV}$) and UV-slope ($\beta$). The

authors describe a EW distribution probability ($P(EW)$) using an exponential model whose parameters (amplitude (A) and e-folding scale ($W_0$)) depend of $M_{UV}$ and $\beta$ in the following way.

$$P(EW_{Ly\alpha}) = \frac{A}{W_0}\mathrm{e}^{\frac{-EW_{Ly\alpha}}{W_0}}H(EW_{Ly\alpha}) + (1-A)\delta(EW_{Ly\alpha}) \tag{3.1}$$

where A and $W_0$ relate with $M_{UV}$ and $\beta$ as:

$$A(M_{UV}, \beta) = A_{M_{UV}}M_{UV} + A_\beta\beta + A_C \tag{3.2}$$

$$W_0(M_{UV}, \beta) = W_{M_{UV}}M_{UV} + W_\beta\beta + W_C \tag{3.3}$$

Coefficients $A_{M_{UV}}$, $A_\beta$, $A_C$, $W_{M_{UV}}$, $W_\beta$ and $W_C$ were fitted by Oyarzun et al. 2017 using a mass-selected sample of galaxies at $z \sim 3.5$ observed with M2FS and selected from the 3D-HST survey (van Dokkum et al. 2013), giving the following values:

$$A(M_{UV}, \beta) = 0.08^{+0.1}_{-0.06}M_{UV} - 0.6^{+0.1}_{-1.2}\beta + 1.1^{+1.5}_{-1.4} \tag{3.4}$$

$$W_0(M_{UV}, \beta) = 11^{+2.0}_{-1.8}M_{UV} - 7.8^{+}_{-5.5}5.2\beta + 235^{+45}_{-42} \tag{3.5}$$

These values were obtained at redshift $z \sim 3.5$, but we assume that the dependence on $M_{UV}$ and $\beta$ remains the same for $z \sim 2.5$ (this work redshift range).

Our procedure for this section is to: (1) measure $M_{UV}$ and $\beta$ for sub-samples of LATIS galaxies in different local density ($\delta f$) bins, (2) estimate the predicted P(EW) of Ly$\alpha$ from the Oyarzun model in each density bin, (3) Compare if the model predicts any changes in P(EW) as a function of $\delta_f$. In order to do that we inspect the predicted P(EW) for each bin, and compare them against the full sample predicted P(EW), as a function of $\delta_f$.

## 3.1 Sample selection

The studies of Ly$\alpha$ emission performed on this section are done with the intention of comparing results with the ones at the following Section 4. The galaxies used in this section are selected considering the conditions needed to conduct the studies in Section 4. These conditions are:

- **Good redshift quality flag:** *zqual* $\geq$ 3. *zqual* is a value taken from the LATIS catalog. A. B. Newman et al. 2020 describe that it is determined by inspecting one by one every target through an interactive GUI, where they try to identify the spectrum and measure an approximate initial redshift, using reference composite spectra and SDSS templates (from Shapley et al. 2003). *zqual* goes from 0 to 4 in the LATIS catalog, where 0 corresponds to the targets where no redshift could be assigned to the spectrum, 1 corresponds to spectra where a single emission was identified and assumed to be Ly$\alpha$, 2 corresponds to low-confidence guess redshift, 3 corresponds to high-confidence redshift, determined by multiple observed lines and a well-modeled

spectrum, and finally 4 corresponds to targets with a certain redshift value, high signal-to-noise spectrum, with numerous lines identified. We use reliable redshifts in this work, filtering $zqual \geq 3$.

- **Not flagged as QSO in the LATIS catalog.** LATIS provides an $isQSO$ flag to identify them from galaxies in the sample. The interactive tool described above allows A. B. Newman et al. 2020 to identify QSOs and create the flag for these type of spectra in the LATIS catalog.
- **Redshift range between** $2.2 - 2.8$. The exact limits are given to be able to measure the Ly$\alpha$ EW directly from the spectra (detailed in Section 4). This range allows us to measure the continuum flux values around the Ly$\alpha$ line for continuum estimation and substraction.
- **A valid** $\delta_f$ **value.** Some galaxies lie in regions of the tomographic volume that do not have enough data to yield a density estimate, usually near the border. It is crucial for our studies to know the local density value of the studied galaxy.

Applying these conditions over the full sample of LATIS, a final sample selection of 1258 galaxies are available to analyze in Sections 3 and 4. For these 1258 galaxies, $M_{UV}$ and $\beta$ are measured as described in following subsection

## 3.2   UV-luminosity ($M_{UV}$) and UV-slope ($\beta$) measurements from available photometry

We estimate $M_{UV}$ and $\beta$ from a power-law fit to the stellar continuum of each galaxy, traced by the available broad-band photometry from CFHTLS (Canada-France-Hawaii Telescope Legacy Survey). The individual galaxy spectra do not have enough S/N nor a long enough wavelength baseline to allow for a significant measurement of these quantities. We must therefore rely on the available photometry.

The photometry available from the final CFHTLS-T0007 release[1] over filters u, g, r, i, z, correspond to the wavelengths and depths in magnitude seen in Table 3.1, depths correspond to 80% completeness limit in AB for each filter. This photometric catalog provides broad-band magnitudes in all these filters.

| Filter | Effective wavelength $\lambda$ | Depth of observations in magnitude |
|:---:|:---:|:---:|
| u | 3543 Å | 26.3 |
| g | 4770 Å | 26.0 |
| r | 6231 Å | 25.6 |
| i | 7625 Å | 25.4 |
| z | 9134 Å | 25.0 |

Table 3.1: Original wavelengths (not rest frame) of available photometry from CFHTLS.

First it is necessary to convert the available magnitudes of the catalog, into the same flux density units of the spectra. : [erg s$^{-1}$ Å$^{-1}$ cm$^{-2}$]. For each galaxy, photometry magnitude

---

[1]http://terapix.calet.org/terapix.iap.fr/cplt/T0007/doc/T0007-doc.html

Figure 3.1: 3 galaxies of the LATIS sample, in color blue: the top panel shows high Ly$\alpha$ emission spectrum example, the medium panel shows a low Ly$\alpha$ emission example, and the bottom panel shows a high UV-slope ($\beta$) example. Spectra are smoothed for visualization. Red dots are available CFHTLS photometry and their error bars transformed into flux. Photometry dots, except the 'u' band, are fitted to $F_\lambda = A * \lambda^\beta$ function to obtain values of $M_{UV}$ and $\beta$, as detailed in section 3.2.

and its errors are transformed into flux density $f_\lambda$, with units erg cm$^{-2}$ s$^{-1}$Å$^{-1}$. Wavelengths are also transformed into rest frame wavelength using the corresponding galaxy redshift from LATIS catalog, and the known formula $1 + z = \lambda_{obs}/\lambda_{emit}$.

After transforming flux and wavelength units, we use the `curve fit` method of Python to set a power-law continuum of the form $F_\lambda = A * \lambda^\beta$, which is fitted to each galaxy spectral energy distribution (SED). Using the photometry values and their errors provided by CFHTLS. Only 4 of the 5 available photometric points were used (g,r,i,z), u-band was left out because it is affected by Ly$\alpha$ emission, the Ly$\alpha$ forest and IGM absorption below the Balmer limit. In figure 3.1 three galaxies from our sample are shown, with high, medium and low Ly$\alpha$ emission values, as a representative of the diversity found in the preliminary LATIS sample. On top of each spectrum, the available photometry is plotted, and also their fitted power-law continuum curve.

The value of $M_{uv}$ magnitude for each galaxy is obtained evaluating the fitted curve $F_\lambda = A * \lambda^\beta$ at $\lambda = 1700$ , and then transforming back this evaluated flux value into an apparent magnitude. Standard error for $M_{UV}$, $\sigma_{M_{UV}}$ are obtained using a Monte Carlo method for error estimation, with N = 3000. Finally the apparent magnitude is transformed into absolute magnitude with the following formula:

$$M = m - DM(z) + 2.5\log_{10}(1 + z) \tag{3.6}$$

where M is the absolute magnitude, m: apparent magnitude, z redshift of the galaxy and DM is the distance modulus at redshift z. Note that the error for the apparent magntude m and absolute magnitude M remains the same (dm =dM).

The value of the UV slope ($\beta$) and its error $\sigma_\beta$ is obtained directly from the `curve fit` output, since is one of the variables of the fitted function (the slope). The distribution of absolute $M_{UV}$ and $\beta$ for the complete galaxy sample can be seen in figures 3.2 and 3.3. Typical UV magnitudes and slopes found in the sample peak around $m_{UV} = -22$ and $\beta = -1.5$. These are typical for LBGs at these redshifts.

## 3.3   P(EW) estimation and how it changes as a function of galaxy properties in different density bins.

Using this obtained values of $M_{UV}$ and $\beta$ from the previous subsection, we can evaluate Oyarzún's model (P(EW)) (3.1) replacing $M_{UV}$ and $\beta$ values into equation 3.4 and 3.5 to obtain $A$ and $W_0$ parameters. The values for coefficients $A_{M_{UV}}$, $A_\beta$, $A_C$, $W_{M_{UV}}$, $W_\beta$ and $W_C$ were determine using the best fit reported in Oyarzun et al. 2017 as shown in equations 3.4 and 3.5. These $A$ and $W_0$ parameters are used in Equation 3.1 to obtain the predicted EW distribution (P(EW)) for each galaxy in the sample. The error in P(EW) ($\sigma_{P(EW)}$) is measured through Monte Carlo method with N = 900 iterations.

Now we are able to use the $\delta f$ values provided by LATIS to divide our sample into "local density bins" combining the P(EW) of all galaxies in each bin to evaluate the EW distribution predicted by the model for the distribution of $M_{UV}$ and $\beta$ in each bin.
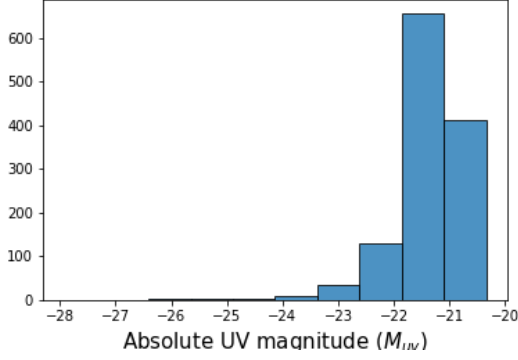
Figure 3.2: $M_{UV}$ histogram of total sample
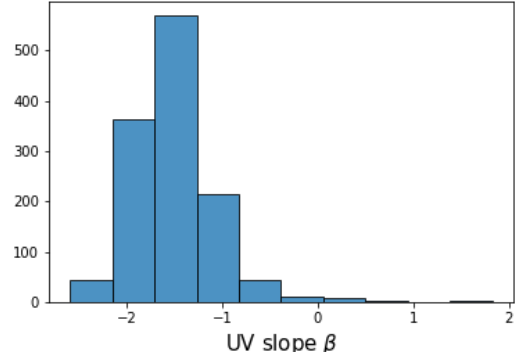
Figure 3.3: $\beta$ histogram of total sample

## 3.3.1   Local density $\delta f$ bins

The distribution of $\delta_f$ for the galaxies is biased towards negative values (i.e. not centered at zero) because galaxies tend to inhabit regions that are denser than the mean density of the universe at all redshfits. Density bins are determined by percentile, the 1258 galaxies of the sample are divided into five bins with the same number of galaxies each. These bins separate the total sample in $\delta_f$ at the 20%, 40%, 60%, and 80% percentiles, and are named as Group 1, 2, 3, 4 and 5 respectively as can be seen in figure 3.4. The limit values of $\delta_F$ for each group are: $0.004 < \delta_F$ , $-0.036 < \delta_F < 0.004$ , $-0.085 < \delta_F < -0.036$ , $-0.145 < \delta_F < -0.085\%$ , $\delta_F < -0.145$. It is important to notice that the values of $\delta_F$ are *smoothed* by a kernel of size $\sigma_{kern} = 2h^{-1}cMpc$.
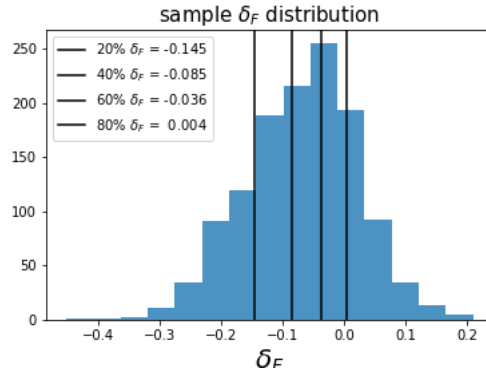


Figure 3.4: $\delta_F$ distribution, vertical lines divide the sample into five percentile bins with the same number of galaxies each, corresponding to $20\%, 40\%, 60\%$ and $80\%$ of the sample respectively.

The $M_{UV}$ and $\beta$ distributions inside each local density bin are shown in figures 3.5 and 3.6 compared to full sample distribution. It can be seen that the five density bins have very similar values for $M_{UV}$ as the complete sample, with peaks around $M_{UV} = -22$. In Figure

21

3.6 it can also be seen similar distributions for all bins, with peaks around $\beta = -1.5$, but a small difference can be detected in the first and last bin. The peak is distributed in a wider range in the first bin, but still centered in -1.5. Also, the distribution seems more symmetrical in the last bin, meaning that it has larger $\beta$ than average.

### 3.3.2 P(EW) as a function of galaxy properties in different density bins.

P(EW) is the probability density of the EW model, meaning that its values are between 0 and 1. If P(EW) $\sim 0$ for some EW, this means that these values are unlikely, given that $M_{UV}$ and $\beta$. P(EW) is described by equation 3.1 and it is evaluated for each galaxy, as described in the previous subsection, using the values of $M_{UV}$ and $\beta$ and their estimated errors, and also evaluated over a range of EW that goes from 0 to 200 (negative values are not defined in this model, so galaxies showing Ly-alpha in absorption are accounted for in the second term of Equation 3.1 at EW=0).

The EW distribution evolves with redshift, and this model was fitted using data at z=3.5, while our galaxies lie at z=2.2-2.8. Although there might be some change in the EW distribution over this range in cosmic time, the relative dependences of the Ly-alpha production and escape as a function of galaxy properties are asumed to hold. We are only interested in the latter.

Figure 3.7 shows the predicted mean P(EW) and its estimated error for all galaxies in each environmental density bin. The main goal with this plot is to explore if there is a significant change between groups. Figure 3.7 shows that no significant differences are seen between the predicted P(EW) for each bin (black solid line) and the full sample (dashed line). In all cases differences are smaller than the $1\sigma$ error in P(EW). This could be happening because galaxies are too similar and the galaxy properties do not change significantly between density groups, as can be seen again in figures 3.5 and 3.6.

This allow us to interpret any changes found in Section 4 as a result of environmental effects and not due internal processes.
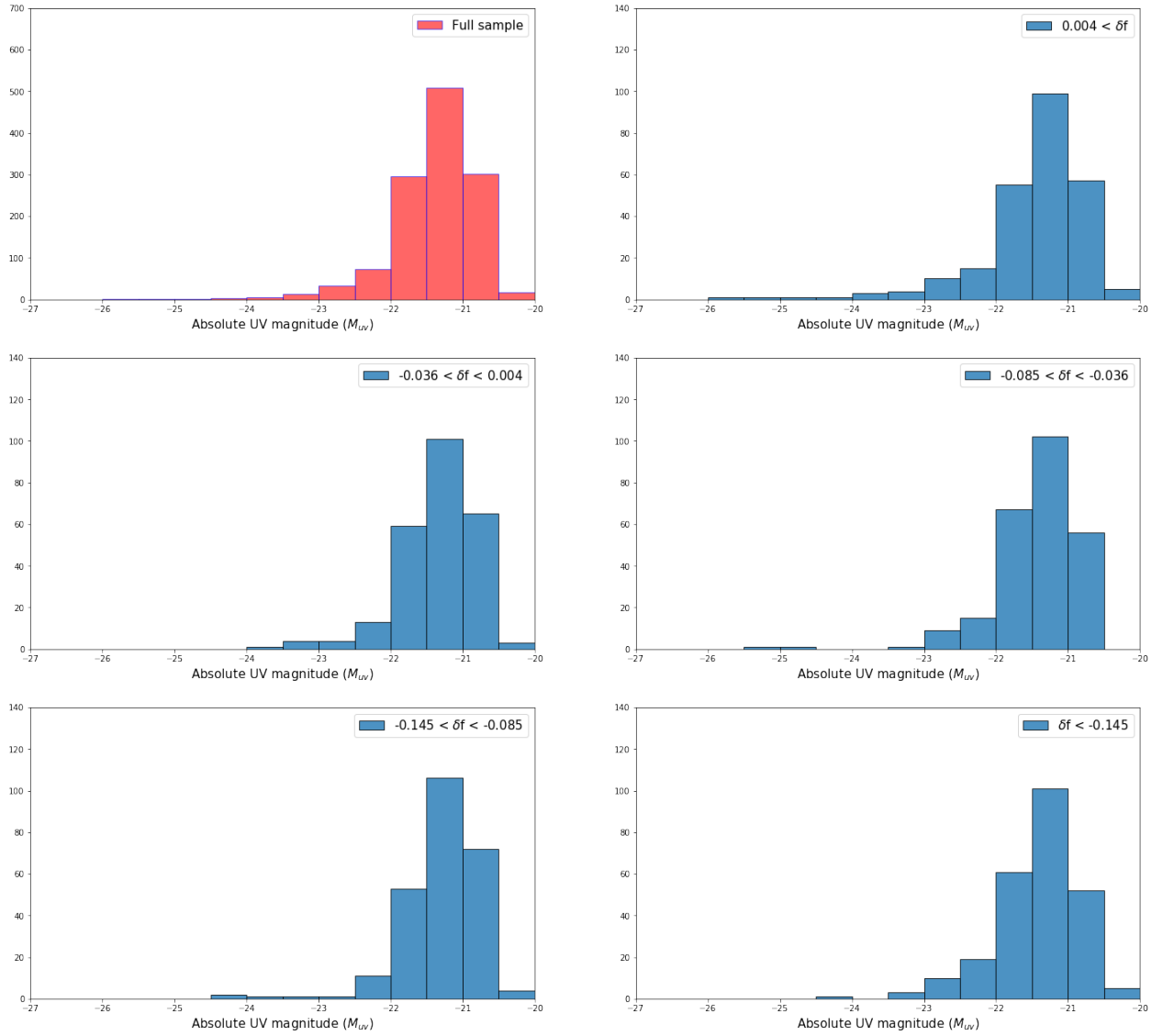
Figure 3.5: $M_{UV}$ histograms of each local density group. It can be seen that the five density bins have very similar values for $M_{UV}$ as the complete sample, with peaks around $M_{UV} = -22$.
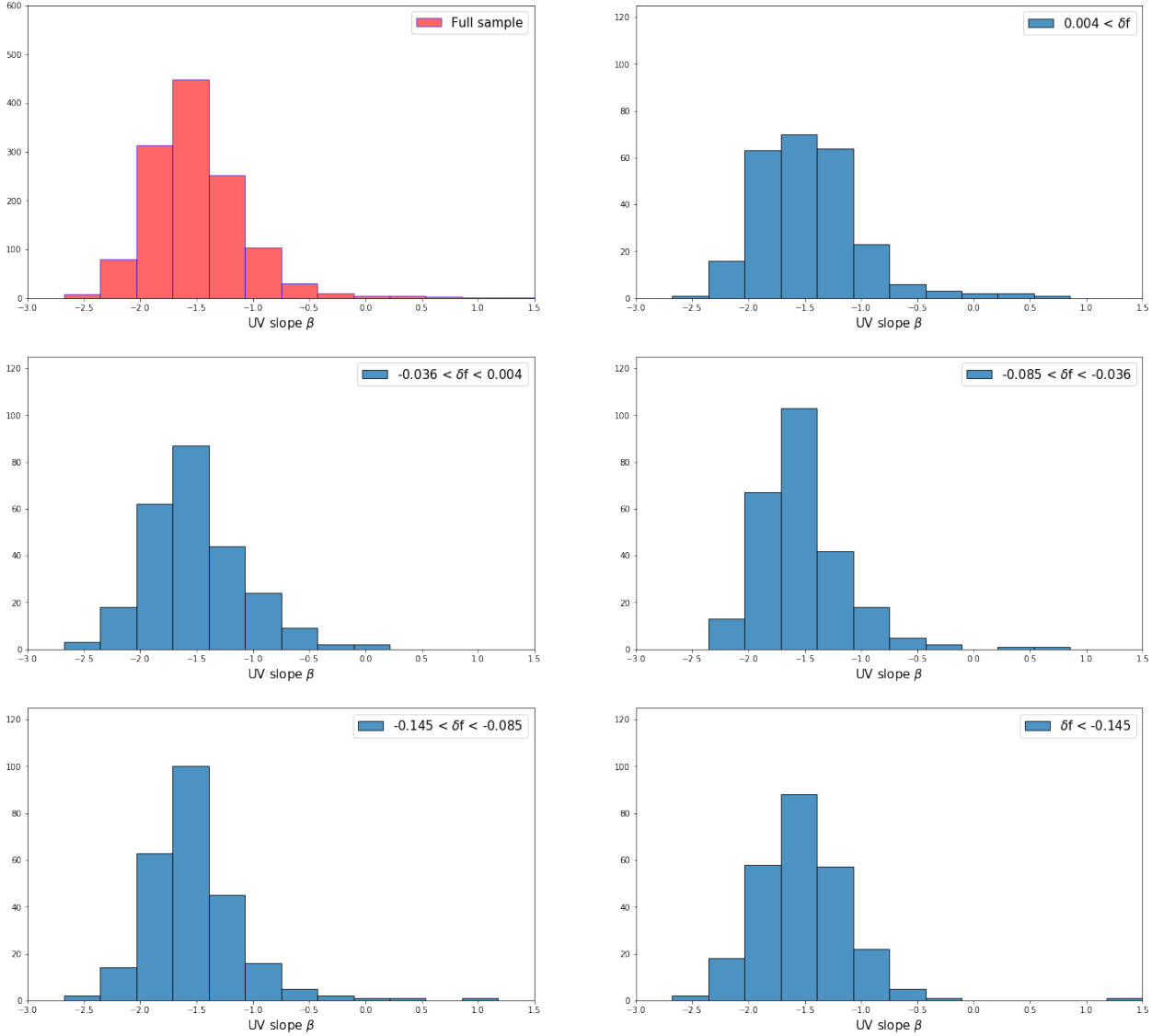
Figure 3.6: $\beta$ histograms of each local density groups. It can be seen similar distributions for all bins, with peaks around $\beta = -1.5$, but a small difference can be detected in the first and last bin. The peak is distributed in a wider range in the first bin, but still centered in -1.5. Also, the distribution seems more symmetrical in the last bin, meaning that it has larger $\beta$ than average.
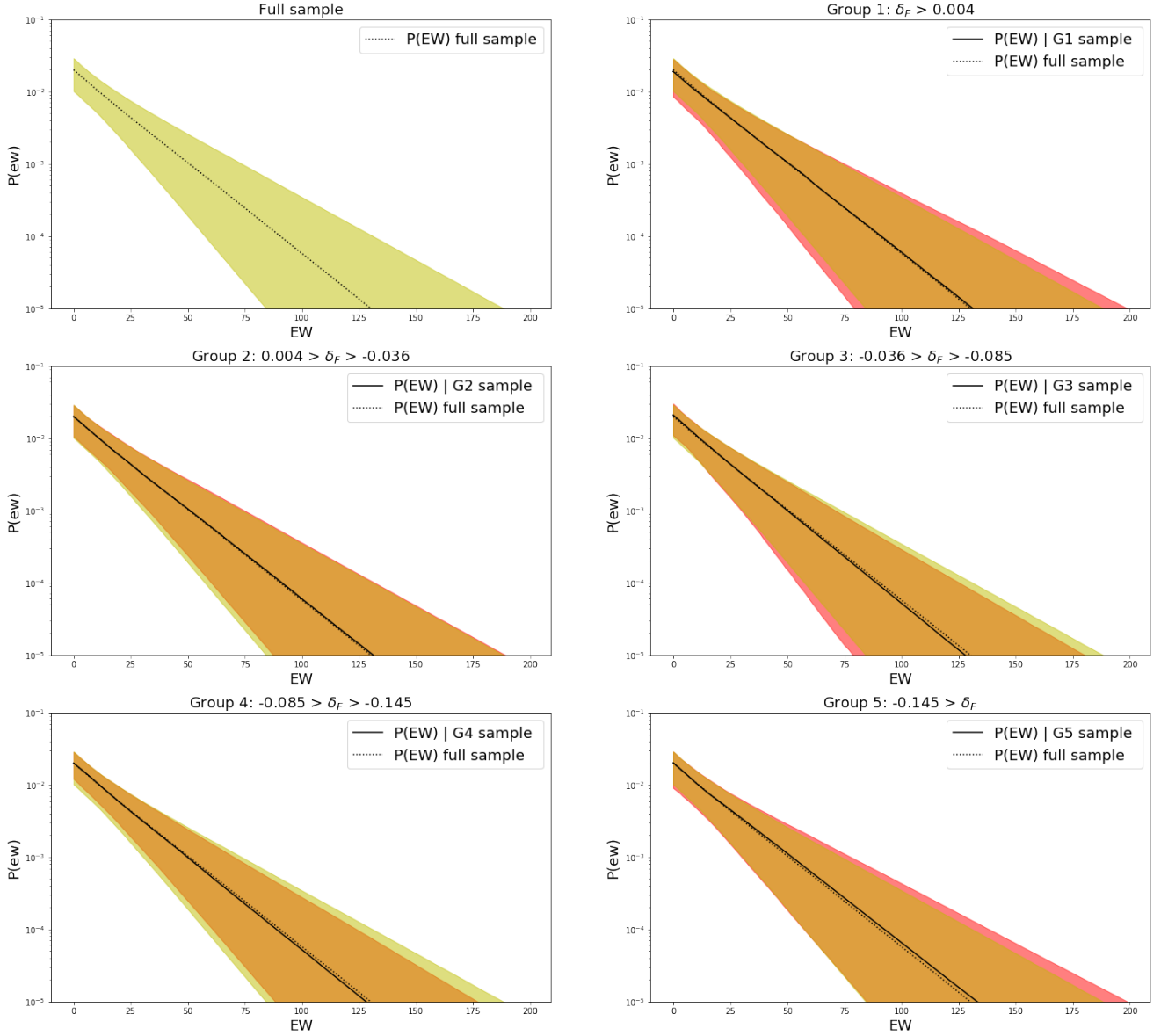
Figure 3.7: Estimated P(EW) for each of the five galaxy groups of local density (solid black line) and their error (red section), compared with the estimated P(EW) for the full sample (dashed line) and its error (yellow section). Top left panel correspond to full sample alone. Top right corresponds to $\delta_f > 80\%$ (G1), the following are $60\% < \delta_F < 80\%$ (G2), $40\% < \delta_F < 60\%$ (G3), $20\% < \delta_F < 40\%$ (G4) , and finally bottom right panel correspond to $\delta_F < 20\%$ (G5). This result shows that differences in predicted EW distribution due to internal properties are not significant (since the black line doesn't change compared with dashed line full sample).

# Chapter 4

# Dependence of Ly$\alpha$ Emssion on Environment

Previous studies of the dependece in Ly$\alpha$ emission with local density show, for example, that Lyman Break Galaxies (LBGs) presenting Ly$\alpha$ in emission show an excess of clustering at intermediate scales of local density (consistent with a shell-like distribution of gas; J. Cooke et al. 2013). This could indicate a preference of Ly$\alpha$ emission to emerge from galaxies in intermediate density environments, avoiding dense environments where possible suppression mechanisms could be in place. These results are based on the study of galaxy auto correlation functions, and therefore rely on environmental information that is not independent of the galaxies themselves.

A major advantage of LATIS (presented in 2.1) is that it provides a measurement of the large scale matter density field that is independent of the galaxies being studied ($\delta_f$). LATIS also provides the spectra of galaxies that inhabit the tomographically mapped structures. Ly$\alpha$ Equivalent Width (EW) can be measured from these provided spectra.

The combination of both $\delta_f$ and EW measurements, provides a unique dataset to study how Ly$\alpha$ emission depends on environment. The large sample size in LATIS allows us to statistically study the shape of the EW distribution with exquisite precision, with hundreds of objects in each of the bins in local matter density. For reference, in Oyarzun et al. 2017 good characterizations of the Ly$\alpha$ EW were obtained with a few dozen objects per stellar mass bin. Furthermore, since LATIS targets a relatively narrow range of LBG luminosities that provide adequate S/N for tomography, most of the galaxy sample has a fairly narrow dynamic range in stellar mass, making it easy to separate bonafide environmental effects from secondary correlations with galaxy properties as shown in the previous section.

In this section we perform studies of Ly$\alpha$ emission of our selected sample pf galaxies (described in 3.1). In particular we are going to study how the Ly$\alpha$ EW distribution changes over the same density bins described in previous section.

## 4.1 Equivalent Width (EW) measurement from galaxy spectra

Equivalent Width (EW) is a measurement of line flux intensity relative to the continuum flux:

$$EW = F_{Ly\alpha}/F_{cont} \tag{4.1}$$

Where $F_{Ly\alpha}$ is the integrated flux of the Ly$\alpha$ line and $F_{cont}$ is the value of the estimated continuum flux density.

The first step is to measure the Ly$\alpha$ EW from the galaxy spectra of our sample. In order to do that we use the method described in Kornei et al. 2010. We start by estimating the underlying continuum from the spectra.

For continuum estimation Kornei et al. 2010 defines two windows in the spectrum, one on each side of Ly$\alpha$ emission line. One window blueward of the line ($C_{blue} : 1120 - 1180$ Å) and the other redward ($C_{red} : 1225 - 1255$ Å). For our studies on emission for this thesis work, we also define these two windows on each side to calculate the average continuum levels, but they are closer to the Ly$\alpha$ line than Kornei's. The main reason to use a closer blue window is to increase the number of galaxies in our selected sample. The original Kornei windows cutoff too many galaxies, since they didn't have observed flux at $\sim 1120$ Åand therefore were filtered out. A closer blue window allow us to incorporate a bigger number of high redshift galaxies. Our continuum windows were defined at $C_{blue} : 1205 - 1213$ Åand $C_{red} : 1225 - 1240$ Å.

Inside of each window an average continuum level is estimated ($C_{blue}*$ and $C_{red}*$) from the galaxy spectrum. Then, the continuum at each wavelength under the Ly-alpha emission line is estimated ($f_c(\lambda)$) by linearly interpolating these two bracketing values ($C_{blue}*$ and $C_{red}*$). This effectively means that we subtract a linear continuum baseline under the line. The $C_{blue}$ and $C_{red}$ windows are shown in figure 4.2 in their respective colors, along with the flux interpolation $f_c(\lambda)$ for three example galaxies in our sample.

Once the continuum is substracted from the spectra, an integral of the spectra flux must be performed around the Ly$\alpha$ line, to obtain the $F_{Ly\alpha}$ value (needed to obtain EW in equation 4.1). In order to do that, we need to define an integration window around Ly$\alpha$ line, where all its flux will be summed up. The Ly$\alpha$ flux is measured through the following equation. 4.2.

$$F_{Ly\alpha} = \int_{1214}^{1221} (f_\lambda - f_c(\lambda))\mathrm{d}\lambda \tag{4.2}$$

Where $f_\lambda$ is the flux from the spectrum, and $f_c(\lambda)$ is the estimated continuum by the linear interpolation between $C_{blue}*$ and $C_{red}*$ described above. The flux difference is integrated around Ly$\alpha$ emission line.

The integration limits are between 1214 - 1221 Å. These integral limits were defined stacking over all the rest-frame spectra of all galaxies with subtracted continuum, and looking
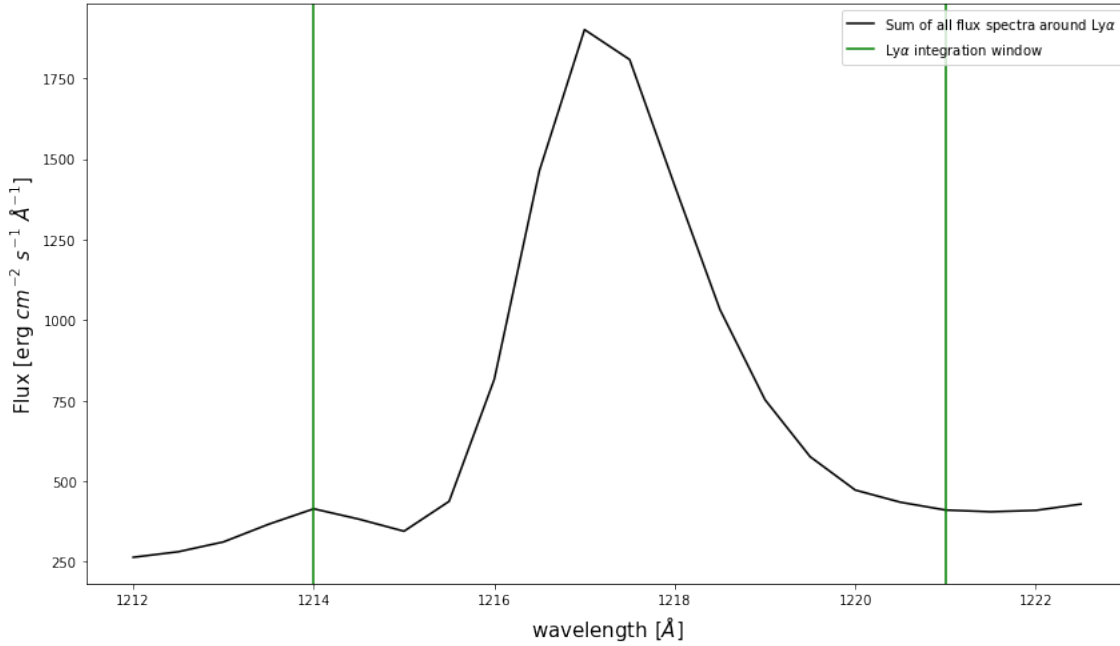
Figure 4.1: Sum of all galaxy spectra, at rest frame, around Lyα emission line. Integration limits to measure Lyα flux are shown. It can be seen that the sum of all galaxy flux resides inside integration window. 98% of the sample has the full Lyα line inside the window.

at the Lyα region. The limits were determined "by eye" to be wide enough to include all the line flux. Figure 4.1 shows the sum of all galaxy spectra flux around the integration limits. Most of the galaxies have the Lyα emission line inside the integration window. With these limits less than 2% of the galaxies ($\sim 20$ of the 1258) have some small portion of the line flux outside the window, we consider this error small enough for the full sample $F_{Ly\alpha}$ estimation. Fig 4.2 shows the integration limits as vertical lines over three example spectra.

After $F_{Ly\alpha}$ is measured, an estimation of the continuum flux $F_{cont}$ is needed. We define another window in the UV range of $1410 - 1520$ of each spectra, and measure the average flux inside that window. Having $F_{cont}$ and $F_{Ly\alpha}$ (4.2) measured we are able now to estimate EW for each galaxy of the sample following the equation 4.1.

Note that EW can be negative in the case where Lyα absorption dominates over emission in the line integration window.
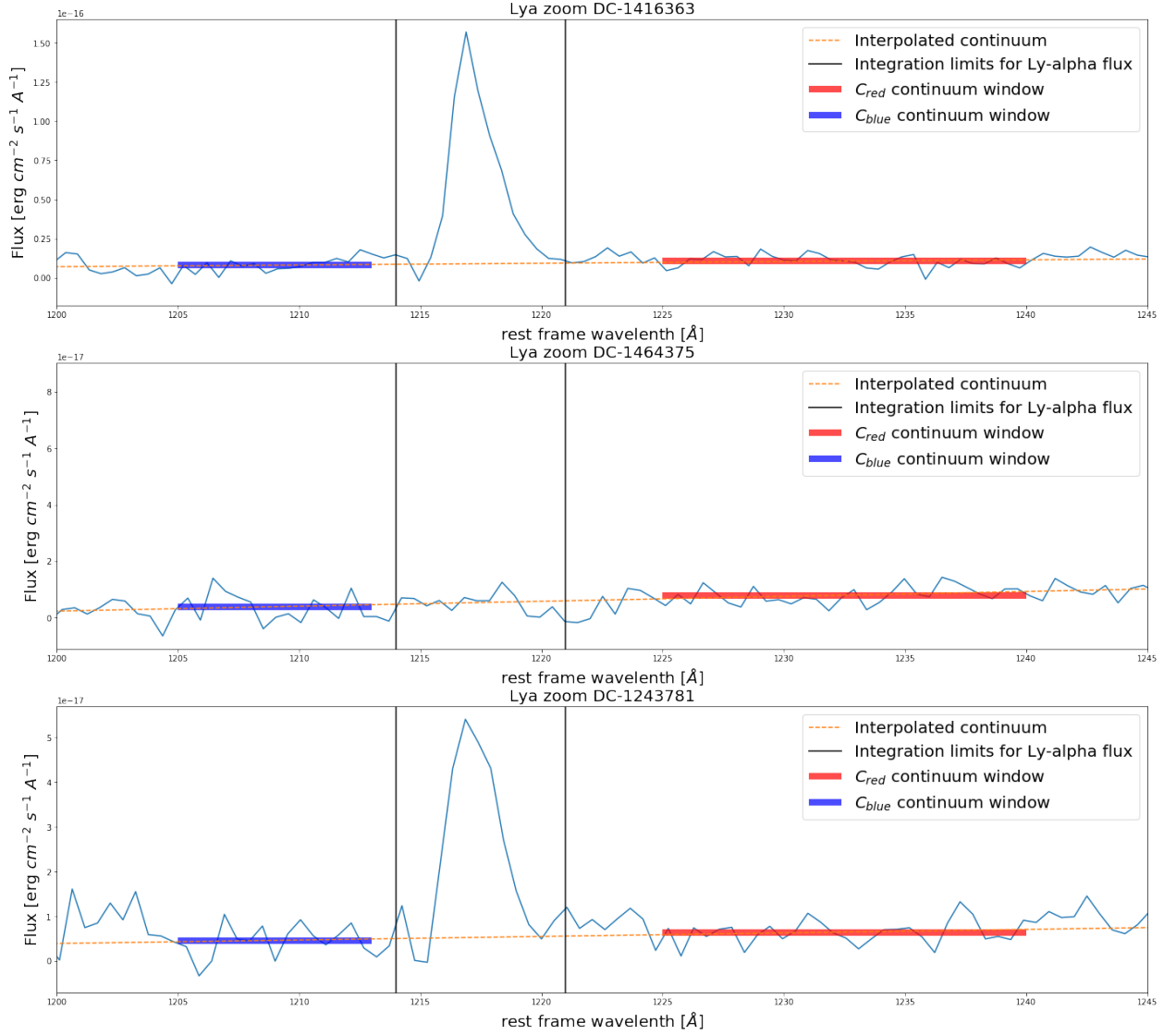
Figure 4.2: Three example galaxy spectra from our sample (the same three galaxies shown in Figure 3.1). The first one corresponds to a large EW example, the second to a low EW and the third to a high $\beta$. Spectra are zoomed into Ly$\alpha$ region. Blue and red continuum windows used for continuum substraction are shown. Integration limits for Ly$\alpha$ flux integration are shown as vertical black lines. Flux interpolation $f_c(\lambda)$ is shown as a dotted orange line.

## 4.2  How the EW distribution changes with local density

We want to study how the EW distribution changes as a function of local density. We therefore divide our sample into density bins the same way as we did in Section 3. That is, we divide the sample by percentiles of $\delta_f$. The 1258 galaxies are divided into five bins with the same number of galaxies each, corresponding to a 20% of the total sample. Density group limits are: $0.004 < \delta_F$ , $-0.036 < \delta_F < 0.004$ , $-0.085 < \delta_F < -0.036$ , $-0.145 < \delta_F < -0.085\%$ , $\delta_F < -0.145$ . A scatter plot of obtained EW vs $\delta_f$ of the sample is shown in figure 4.3.

Figure 4.3 shows that most galaxies have EW < 15 Å. While at first sight it might appear that high EW galaxies only inhabit environments with intermediate densities, this might be caused by a stochastic sampling effect. As seen in the right histogram, the total number of galaxies at intermediate densities is larger, and therefore it might be simply be more likely to sample the high EW tail of the EW distribution, even if galaxies are drawn from the same distribution at all values of $\delta_f$.

EW distributions in each local density bin are measured separately. In order to check whether the EW distributions change as a function of density we fit them using a simple model and we study how the model parameters change for different environmental density bins. A simple exponential model has been found to be a good representation for the Ly$\alpha$ EW distribution in the literature (Oyarzun et al. 2017, Blanc et al. 2011). The exponential model is described by the following equation 4.3 :

$$P(EW) = A * \mathrm{e}^{(-EW/b)} \tag{4.3}$$

Where $A$ corresponds to the amplitude of the exponential and $b$ to the *e-folding*. We fit these exponential functions to each EW distribution corresponding to a group of local density, as seen in figure 4.4.

After fitting the exponential curve, we compare the best-fit exponential model parameters, amplitude and *e-folding* scale (and their uncertainties), across our different density bins, to check whether statistically significant variations are observed. Figures 4.5 and 4.6 show these comparisons between fitted parameters in different local density groups. The values of the parameters are all consistent within the error bars. We find no statistically significant changes in the EW distribution of Ly$\alpha$ emission as a function of density for galaxies in the sample. This is one of the main results of this study.
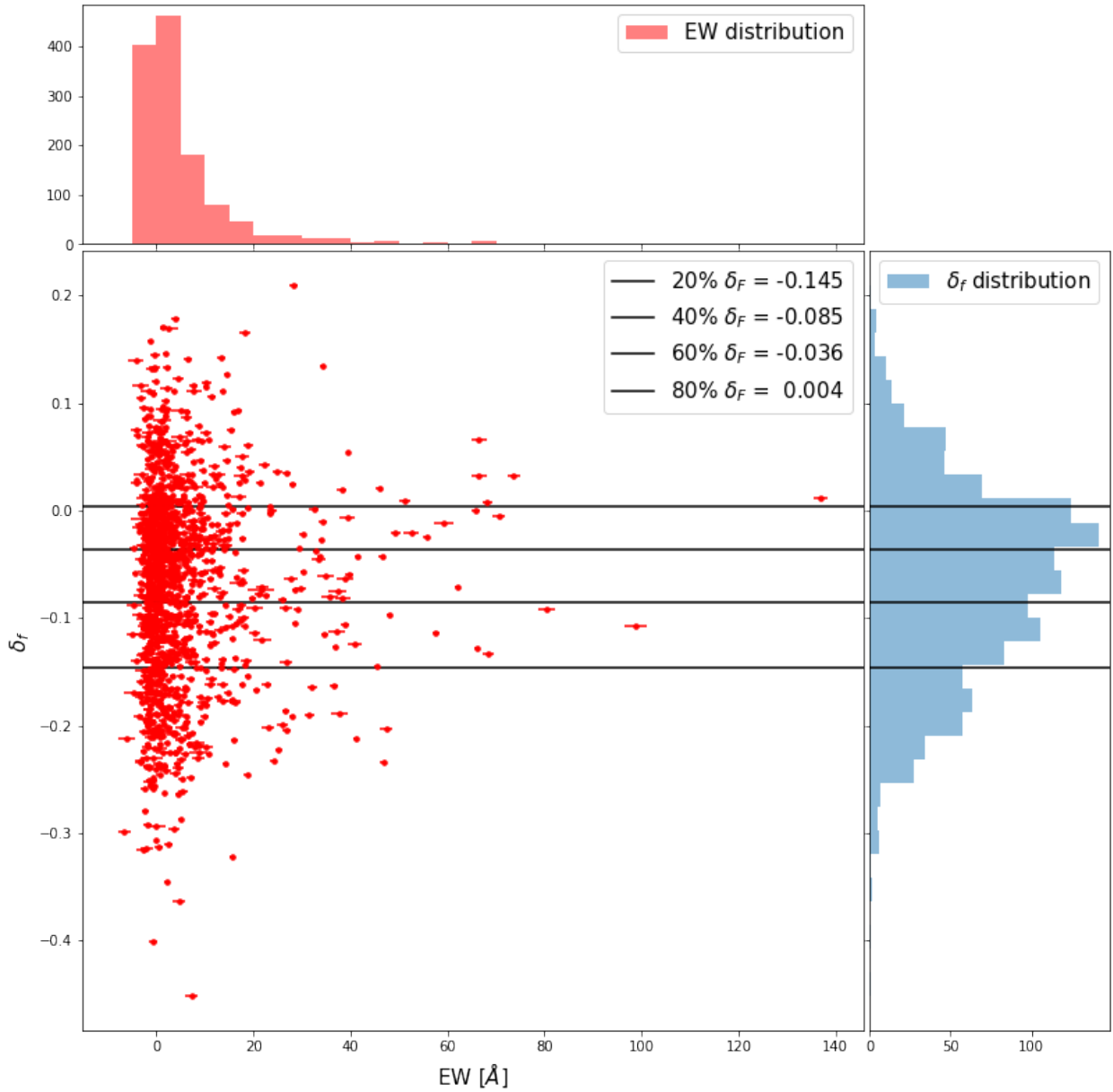
Figure 4.3: EW distribution and $\delta_f$ distribution of studied sample. Scatter plot of both values is shown in red dots. The black lines show the division of the sample into percentile density bins.
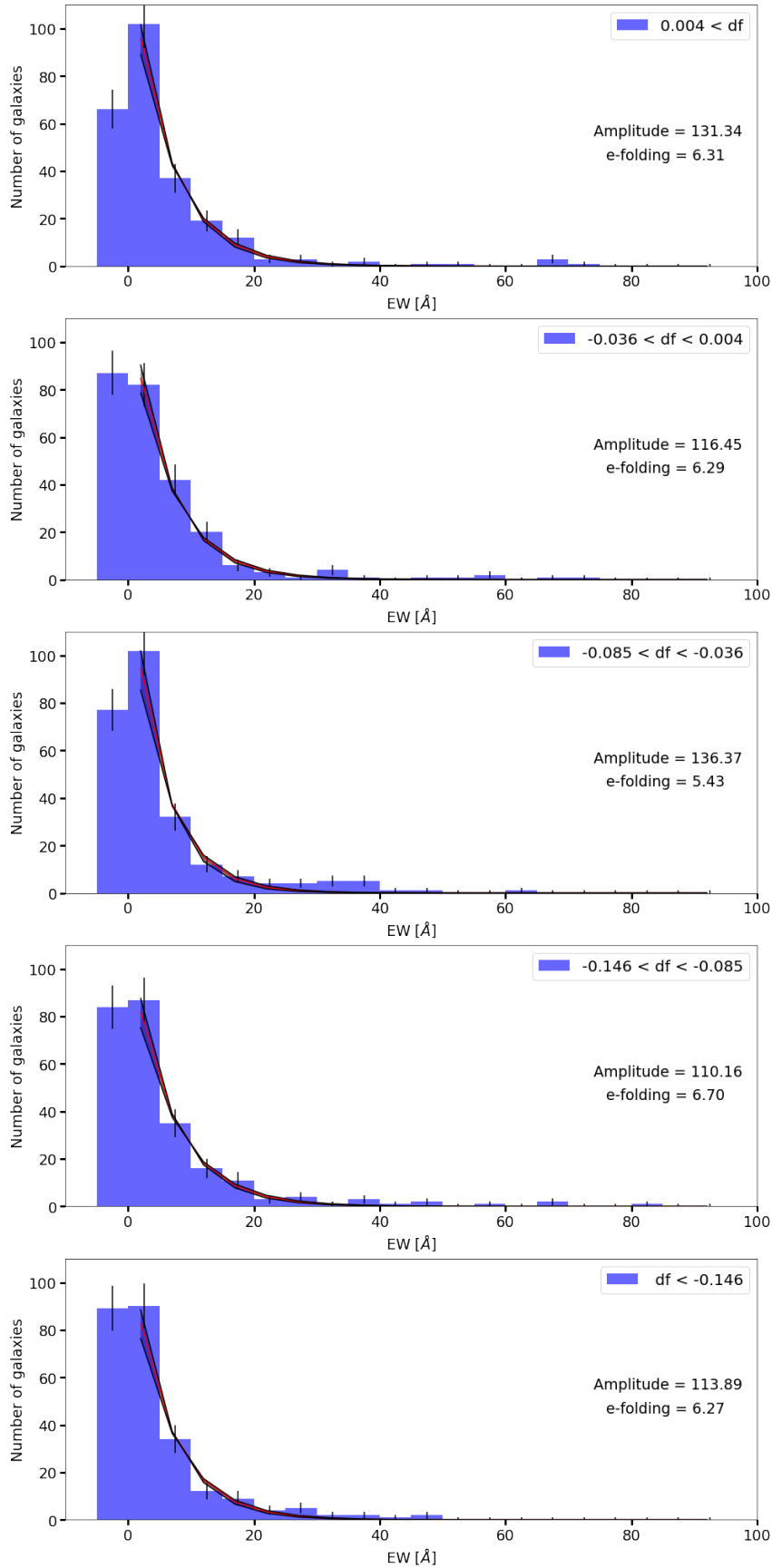
Figure 4.4: EW distribution of each density bin. An exponential function (4.3) is fitted to have a measure of how it changes bin to bin. There are no evident changes looking directly to the distributions. Analysing the changes in the fitting parameters could confirm this observation.
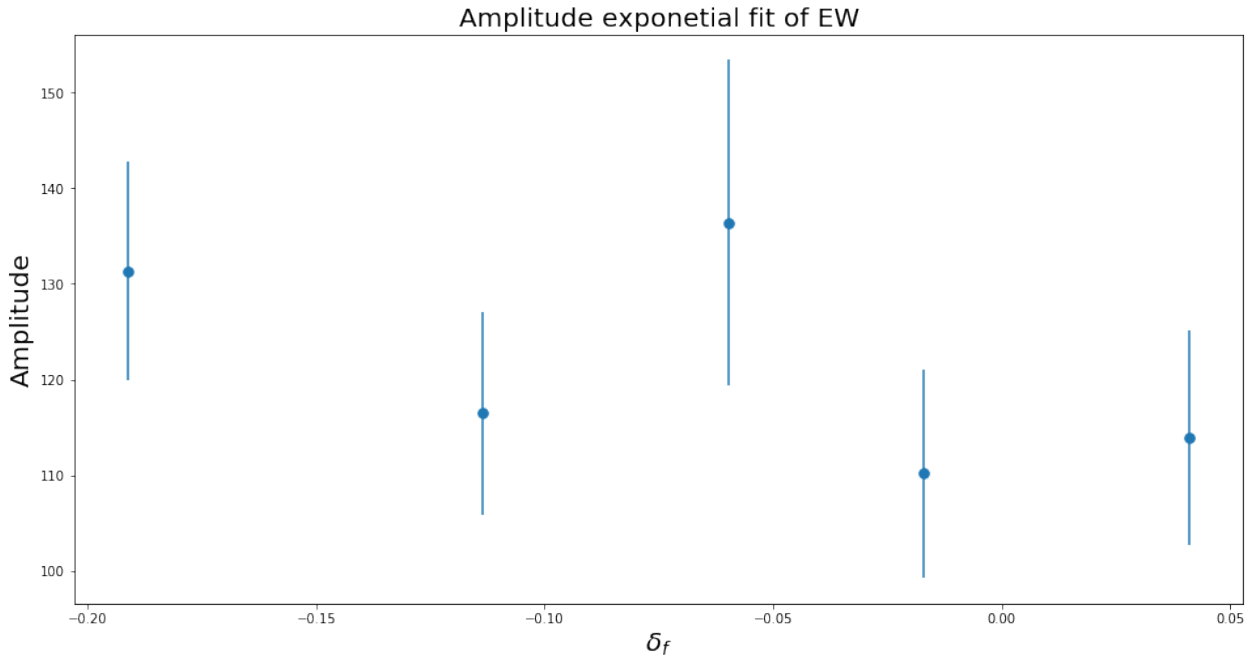
Figure 4.5: Amplitude of exponential fit to EW distribution for each bin of $\delta_f$. The values are consistent with the error bars. No significant change is detected though different local densities.
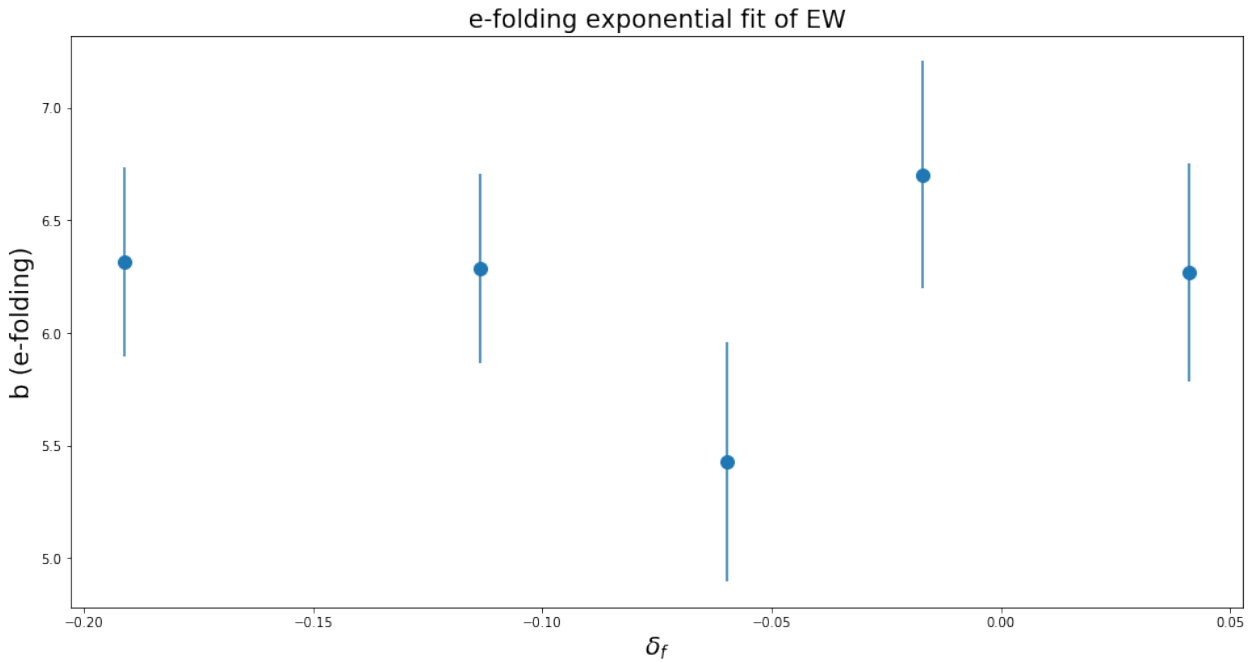


Figure 4.6: e-folding of exponential fit to EW distribution for each bin of $\delta_f$. The values are consistent with the error bars. No significant change is detected though different local densities.

**K-S test**

To verify that EW distributions do not change over different bins we also perform a Kolmogorov-Smirnov test (KS test) comparing the EW Cumulative Distribution Functions (CDFs) of different bins with each other.

K-S test compares the equality of two data sets of CDFs. It does not assume a predetermined distribution. The test propose a *null hypothesis*: "What is the probability that these two sets of samples were drawn from the same (but unknown) probability distribution?". The test gives a numerical probability for rejecting the null hypothesis. When performed, it returns a D statistic and a p-value. D statistic is the supremum of the distances between the CDFs of the two samples, the closer this number is to 0 the more likely it is that the two samples were drawn from the same distribution. P-value is used to quantify the statistical significance of the D statistic, under the assumption that the null hypothesis is correct. If p-value is smaller than the typical treshold ($p < 0.05$) the null hypothesis can be rejected. On the other hand, if the p-value is higher than 0.05, there is no significant statistical evidence to reject the null hypothesis.

In this case we run a K-S test for each possible pair between the five studied EW CDFs on each local density bin. We want to prove that the null hypothesis can not be rejected, and therefore the CDFs are drawn from the same distribution with high probability. We expect small D statistics, meaning that CDFs are similar, and a high p-value, meaning high statistical significance of the D statistic values, assuming that the null hypothesis is true.

After running the K-S test comparing each bin with each other, we obtain values reported in the following table:

| compared groups | D-statistic | p-value |
|:---:|:---:|:---:|
| EW1 - EW2 | 0.079 | 0.391 |
| EW1 - EW3 | 0.077 | 0.427 |
| EW1 - EW4 | 0.095 | 0.192 |
| EW1 - EW5 | 0.115 | 0.065 |
| EW2 - EW3 | 0.070 | 0.544 |
| EW2 - EW4 | 0.043 | 0.966 |
| EW2 - EW5 | 0.087 | 0.279 |
| EW3 - EW4 | 0.074 | 0.468 |
| EW3 - EW5 | 0.086 | 0.296 |
| EW4 - EW5 | 0.091 | 0.233 |

Table 4.1: Reported values of K-S test (D statistic and p-value ) between EW CDFs of each bin.

As observed in table 4.1, all D statistic values were around 0 and 0.1 max, meaning that CDFs are similar. Obtained p-values are high ($p > 0.2$ in most cases, and the lower is still bigger that 0.05), meaning high statistical significance of the D statistic values, assuming that the null hypothesis is true. So we finally confirm qith high probability that there is no changes in EW distriutions measured in different environments across the galaxy sample.

### 4.2.1 Expectation from Theory

Our main goal for this section was to explore if there is a dependence of observed Ly$\alpha$ emission over different density environments. We used as a main tool the Ly$\alpha$ Equivalent Width distribution to characterize the Ly$\alpha$ emission. In order to study the impact of environment, we looked for changes on separate EW distributions, in bins divided according to their local density measure ($\delta f$), finding that there are no statistically significant changes in the EW distribution of Ly$\alpha$ emission as a function of local density.

We may have expected to find some kind of variation between different environments, assuming that stronger scatterings and effects over the emission could take place in denser regions, but as stated in the previous subsection, no significant trend was found. This might be related to the type of galaxies used for the study: the preliminary set of galaxies provided by the LATIS project. LATIS galaxies are massive LBG ($\sim 10^{10} M*$ ) and live in large haloes ($M_{halo} \sim 10^{12} M*$ ). Theoretical studies predict that the dependence of $Ly\alpha$ emission properties over environment are different for galaxies residing in halos of different masses (Zheng et al. 2011).

Zheng et al. 2011 studies how Ly$\alpha$ Radiative Transfer (RT), depends on the IGM density and velocity structure around Ly$\alpha$ emmitting galaxies (LAEs). The authors use cosmological simulations with radiative transfer calculations to track the suppression of Ly-alpha emission ($L_{apparent}/L_{intrinsic}$). In particular, Zheng et al. 2011 focuses on studing the clustering of $z \sim 5.7$ LAEs in a cosmological reionization simulation, focusing on the effects of Lya RT on their clustering properties.

Zheng et al. 2010 presents a simple physical model of LAEs where RT is the primary physical process transforming intrinsic to observed Ly$\alpha$. This was done through a cosmological reionization simulation that considers a complete RT model at redshift $z = 5.7$. The simulation has a box size of 100 h$^{-1}$ Mpc on a side. In the calculation of RT, a $768^3$ grid is used to represent the neutral Hydrogen density, temperature, and peculiar velocity fields in the simulation box. The Hubble flow is added to the velocity field. LAEs are assumed to reside in dark matter halos with positions and velocities from the simulation's halo catalog. To reduce source blending in the Ly$\alpha$ image and spectra, Ly$\alpha$ photons are collected with a finer spatial resolution, a $6144^2$ grid for the image of the whole box, corresponding to 16.3 h$^{-1}$ kpc (comoving) or 0$''$.58 per pixel.

In the first section of Zheng et al. 2011 the authors measure the Ly$\alpha$ suppression ($L_{apparent}/L_{intrinsic}$) in their cosmological galaxy simulation and compare how this quantity varies over four physical variables related to environment: mass overdensity ($\delta$), its gradient along the line of sigth ($\frac{\partial \delta}{\partial z}$), line-of-sigth halo peculiar velocity ($v_{z,halo}$) and peculiar velocity gradient along the line of sigth ($\frac{\partial v}{\partial z}$), separately for four subsets of halos divided according to their halo mass. (see fig: 4.7).

This studied mass overdensity $\delta$ in Zheng et al. 2011 is correlated with the flux overdensity $\delta_f$ reported by LATIS. As an example of this correlation we can see Lee, J. F. Hennawi, et al. 2016 paper, which shows in Figure 8, that lower de$lta_f$ implies more absorption and also higher matter overdensity. Therefore, fot the analysis of this section we observe these trends with overdensity reported in Zheng et al work as a equivalent trends with de$lta_f$.

In general, $Ly\alpha$ suppression is weaker in regions of lower density, the suppression depends on the sign of the density gradient along the line of sight, in the sense that sources located in the near side (with respect to the observer) of an overdense region have a lower suppression.

It is interesting to notice how the dependence of RT with environment also depends on halo mass. It is seen in Figure 4.7 that the overall dependence on environment becomes weaker for sources in halos of higher mass. Probably indicating that $Ly\alpha$ scattering encountered in virialized regions or their immediate surrounding, which are less affected by environments, becomes more important for higher mass halos.

Even though in general Zheng et al. 2011 predicts environmental dependencies in RT and hence on observed-to intrinsic luminosity, those predictions apply mainly to lower mass galaxies. Compared with our results on $Ly\alpha$ emission dependence on environment, we can reaffirm that not finding any trend might be related to the fact that the LATIS targets are LBG with high mass halos. Our results are consistent with Zheng et al. 2011 predictions, but that doesn't mean that the environment does not affect $Ly\alpha$ emission, it means that for high mass galaxies environment is not a predominant effect.
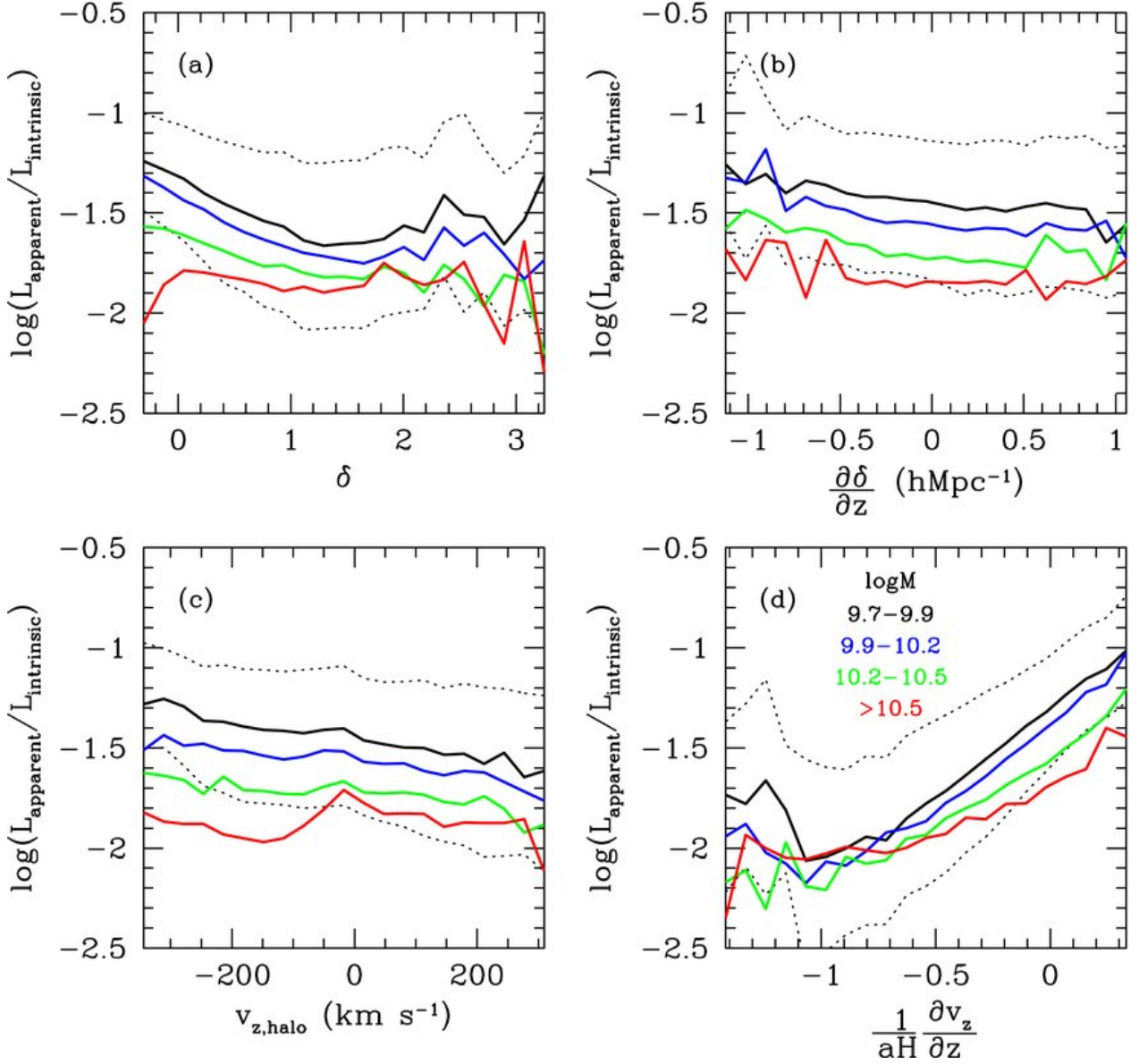
Figure 4.7: Zheng et al. 2011, Figure 1. Dependence of Ly$\alpha$ flux suppression of LAEs on density and peculiar velocity, as a function of halo mass. The suppression is characterized by the ratio of the apparent (observed) and intrinsic Ly$\alpha$ luminosity $L_{apparent}/L_{intrinsic}$. (a) Dependence on the smoothed overdensity field at the source position. The overdensity field is smoothed with a 3D top-hat filter of radius 2 h$^{-1}$ Mpc (comoving). (b) Dependence on the density gradient along the Z-direction. The derivative is with respect to comoving coordinate. (c) Dependence on the host halo velocity. (d) Dependence on the linear peculiar velocity gradient along the Z-direction. The linear peculiar velocity is obtained from the smoothed overdensity field based on the continuity equation (see the text for details). The velocity gradient is put in units of the Hubble parameter. Different colors are for LAE host halos of different masses, as labeled in panel (d). The median of the ratio is plotted as a solid curve. The two dotted curves delineate the upper and the lower quartiles, and for clarity we only plot those for the lowest mass range. Note that the line-of-sight direction (from the observer to sources) is along the Z-direction.

# Chapter 5

# Dependence of Ly$\alpha$ absorption on Environment

Lyman Break Galaxies (LBGs) generically present a damped Ly$\alpha$ absorption line in their spectra produced by their own starlight passing through the Interstellar Medium (ISM) and Circumgalactic Medium (CGM) and being absorbed by their gas, mainly neutral Hydrogren (HI). Around galaxies, HI does not completely cover the starlight, it is not homogeneously distributed, so some light passes through relatively unabsorbed lines of sight. In the simplest picture (the so-called picket-fence model, Heckman et al. 2011), the situation can be described by a covering fraction (the percentage of the galaxy that is covered by gas) and the column density of HI in the covered parts. Both the covering fraction and the column density can be measured from galaxy spectra following the results from Reddy et al. 2016. Using a model of partial covering fraction it is found that galaxies with redder UV continua have a larger covering fraction of HI and dust, with a higher line-of-sight dust column density. It is also found that the absolute escape fraction of Ly$\alpha$ emission, correlates inversely with neutral gas covering fraction, among other results.

In this section we explore whether large scale environment has an impact on the Ly$\alpha$ absorption observed in galaxy spectra. We are interested in knowing whether the environment has an impact on the properties of the circumgalactic gas, or the clustering of neighbouring halos, or the ISM of galaxies, or any physical cause for the observed Ly$\alpha$ absorption. In order to do that we use LBGs from the LATIS sample, where we can measure the absorption spectrum in a relative sense in different large-scale environments.

## 5.1   Sample selection

To perform the mentioned absorption studies, we don't need to cover a blue continuum window to measure the emission EW, so for this section we can have a slightly bigger sample, selected considering the following conditions:

- Good redshift quality: $zqual \geq 3$. $zqual$ is a value taken from LATIS catalog, it goes from 0 to 4 and numbers above 3 imply high confidence redshift value declared for the

galaxy.

- Filter QSOs from LATIS catalog. LATIS provides an isQSO flag to identify them from the complete sample.
- A valid $\delta_f$ value. Some galaxies lie in regions of the tomographic volume that do not have enough data to yield a density estimate, usually near the border. It is crucial for our studies to know the local density value of the studied galaxy.

A final sample of 1771 galaxies are selected using this criteria.

## 5.2 Ly$\alpha$ Absorption in LATIS Galaxies

Absorption studies are done by measuring it against the continuum of the spectra. We can't do individual measurements of absorption as we did for emission studies in the previous section, as the continuum of our galaxies is so faint that the signal-to-noise (SN) of the spectra makes it impossible to make a robust reliable measurements of how much absorption there is in individual galaxies.

To explore the absorption in our sample spectra, we construct Figure 5.1 by plotting all galaxy spectra in a color plot sorted by local density on y-axis. Adjustments made for each variable to create the plot are described in following subsections:

### 5.2.1 Spectra Wavelength

In figure 5.1, the spectra are transformed into their rest frame using available redshift estimation, and then restframe wavelength in Å, is transformed into restframe velocity $\Delta V$ in km/s following equation:

$$\frac{\Delta v}{c} = \frac{\Delta \lambda}{\lambda} = \frac{\lambda_r - \lambda_0}{\lambda_0} \tag{5.1}$$

where $\lambda_0 = 1215.67$ , Ly$\alpha$ wavelength.

After transformation from wavelength to velocity, spectra are interpolated for plotting with the same number of points on the $x$ axis of the plot.

### 5.2.2 Spectral Flux

The LATIS tomographic reconstruction, as described in section 2.4, select galaxies that are surrounded by more or less Ly$\alpha$ absorption to define the environment measure $\delta_f$. So if we compare the average spectrum flux of galaxies in different bins of de$lta_f$, we have to find that there is more Ly$\alpha$ absorption near galaxies in bins of lower de$lta_f$. This is how the bins are defined in the first place.

In this section, we want to isolate and study what differences there might be in absorption in different environments at galaxy scales. By dividing out the large-scale absorption determined from the tomographic maps, we take out these known differences. Therefore,

the flux of each spectrum is corrected by the foreground Lyα transmission along the line of sight, as measured in LATIS tomographic reconstruction. This removes the large scale (> 2 Mpc) foreground IGM absorption from the spectra, leaving only the local absorption signal associated with the local environment in which the galaxy inhabits.

Then, all galaxy spectra are normalized by their mean flux on the range $1235 - 1241$ Å, which correspond to $4700 - 6250$ km/s, as a reference point for the UV continuum (See vertical red lines on figure 5.1). Differential absorption is going to be measured against the value of the continuum in this range.

### 5.2.3 Galaxy local density ($\delta_f$)

Finally, all galaxy spectra are sorted by their local density ($\delta_f$) on the vertical axis of the plot.
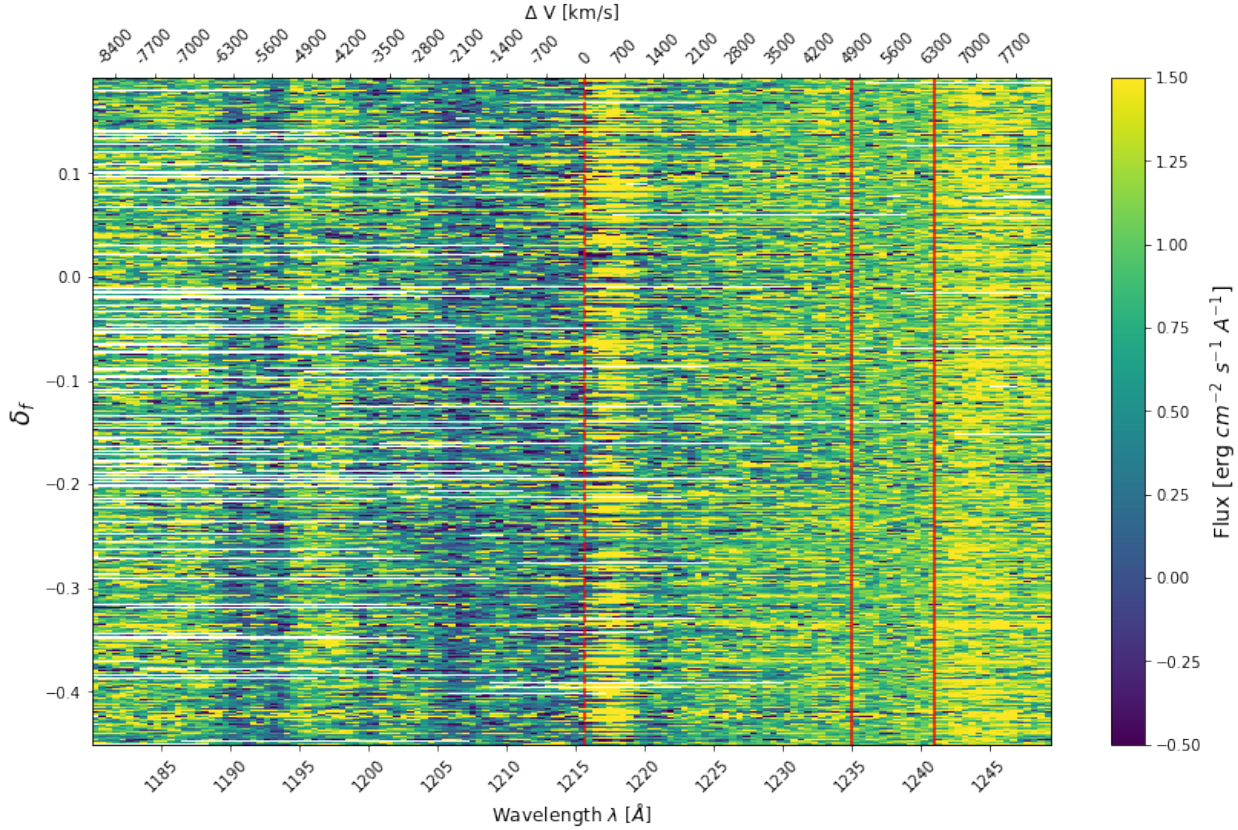


Figure 5.1: All galaxy spectra of sample sorted by $\delta_f$, without any smoothing. x-axis is presented both in wavelength [Å] and $\Delta V$ [km/s] units, the latter corresponds to a Velocity dispersion with respect to Lyα emission line. Red solid lines mark UV side of the spectra used for flux normalization. Red dashed line marks Lyα emission wavelength. Lyα emission is easily observed redshifted from $\lambda \sim 1216$ Å.

By inspecting figure 5.1 we can see that Lyα emission is redshifted, observed from 0 km/s and extended up to $\sim 700$ km/s, but absorption features around Lyα emission are very noisy.

In order to increase SN, the same plot is made but with an additional "smoothing", done by taking the median flux over a number of galaxies in the y axis of the plot. The smoothing is represented by a kernel of dimension $b$ = number of galaxies. Different values were tested for this smoothing, where finally a kernel of $b = 50$ was selected as a good size to recover Ly$\alpha$ absorption features. The smoothed version of the plot can be seen in figure 5.2
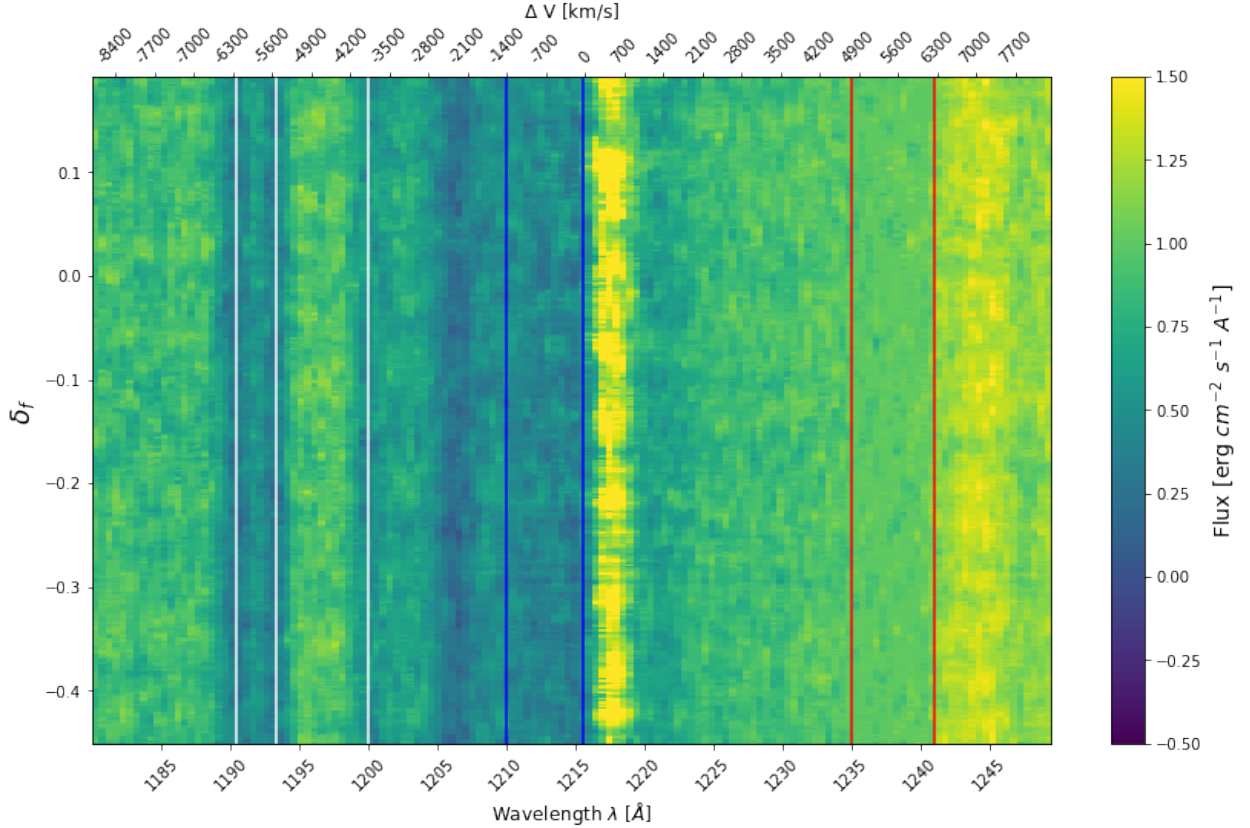


Figure 5.2: All galaxy spectra of sample sorted by $\delta_f$. All spectra are normalized by UV range flux (red lines). x-axis is presented both in $\Delta V$ [km/s] and wavelength [Å] units. Color scale corresponds to normalized flux. Galaxy spectra are also smoothed using a $b = 50$ kernel that takes the median flux over 50 galaxies. White lines correspond to the position of known metals found in all galaxy spectra: SII doublet (1190.4 and 1193.3 Å) and NI (1200.0 Å). The blue lines represent the section where we study absorption effects (see section 5.3).

## 5.3   How observed Ly$\alpha$ absorption changes with $\delta_f$

In figure 5.2 absorption is clearly observed to the left/blue of Ly$\alpha$ emission. It is dispersed over a broad range of velocity, with a full width half max $\sim 700$ km/s. This value is larger than expected from the circumgalactic gas motions, typically around 300 km/s (Rudie, C. C. Steidel, Trainor, et al. 2012). From a physical perspective, it is really uncommon for an atom to be able to absorb a photon 100s of km/s away from the central absorption wavelength. When velocities are observed as this wide range, it is always interpreted as damped absorption. Damped absorption in galaxies occurs when there is a very high column density

present. In this condition, the low probability of this high velocity absorption is canceled out by the big number of atoms. This is consistent with Reddy et al. 2016.

We want to check on this observed broad absorption and check if it changes with $\delta_F$. In order to do that we first divide the complete sample in local density bins as we did in previous sections. Density bins are determined by percentile, the total number of galaxies of the sample (1771) are divided into five bins with the same number of galaxies each, named as Group 1, 2, 3, 4 and 5. The limit values of $\delta_F$ for each group are: $0.003 < \delta_F$ , $-0.038 < \delta_F < 0.003$ , $-0.082 < \delta_F < -0.038$ , $-0.139 < \delta_F < -0.082\%$ , $\delta_F < -0.139$.

For each bin, the median flux inside the adopted "absorption window" (blue) is measured. This window corresponds to the velocity range of $-1400$ to $0$ km/s (blue lines on Figure 5.2). This range was selected because even though absorption is observed both to the blue and red side of Ly$\alpha$ emission, the latter is redshifted, contaminating the red side absorption. The blue side of Ly$\alpha$ absorption is cleaner to study.

The value of the measured median flux inside the absorption window (blue window) is plotted in figure 5.3.
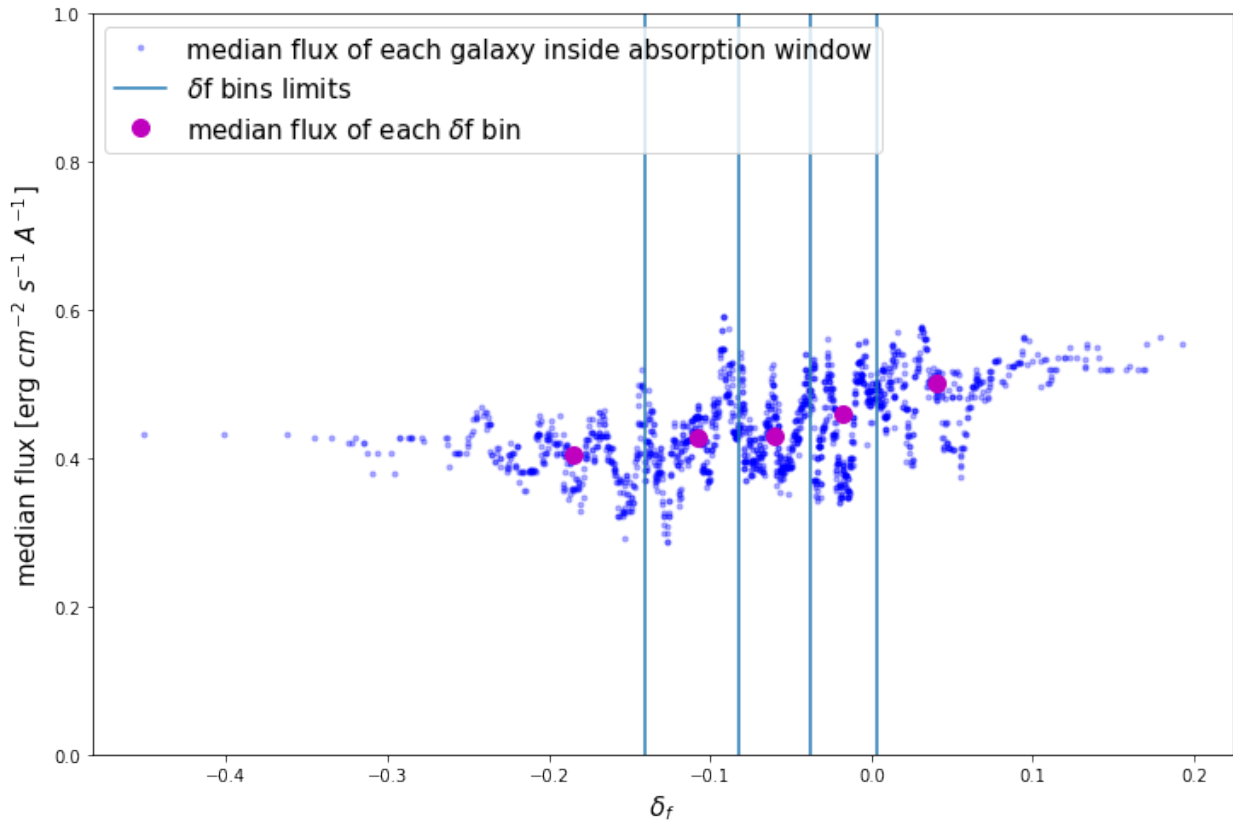


Figure 5.3: Median flux of each galaxy inside absorption windows (blue dots). Magenta dots are median flux for each of $\delta_f$ bin. Light blue lines are the limits for local density bins

Figure 5.3 shows the median flux of each galaxy spectra inside the blue window (aborption

window) of each galaxy spectra. Light blue vertical lines show the limits of local density bins. Big magenta dots represent the median flux of each local density bin in the absorption window. There is an observed trend over the level of absorption changing with $\delta_f$. The flux increases, absorption decreases, as environmental density is decreasing.

In order to take a more detailed look at this trend, and to try to understand why it is happening, we proceed to study stacked galaxy spectra for each group of local density.

## 5.4 Differential absorption observed on stacked galaxy spectra and how it changes with $\delta_f$

Using the same density bins as in the previous sub-section we now create stacked galaxy spectra for each bin. In this section we are normalizing $\delta_f$ values by the map standard deviation $\sigma$. All galaxy spectra are also normalized by the median flux value over $1300-1500$ Årange. Galaxies corresponding to a certain bin are then stacked taking the median flux value on each wavelength, and the resulting stacked spectra is then smoothed by 5 pixels only for visualization. This procedure is repeated for each group of galaxies creating a stacked spectra for each bin and then plotted in Figure 5.4. Errors in each stacked spectra are calculated by taking 50 bootstraps.

Figure 5.4 does not show a clear trend over the absorption feature to the left of Ly$\alpha$ emission. For a better visualization of the absorption, the ratios between the stacked spectra of each bin versus the first bin are taken. By doing this we get a representation for **differential absorption** for each group with respect to the first one, as shown in Figure 5.5. Here we can easily observe some differences between the ratio curves that are bigger than error bars. Next step will be characterize these curves by fitting an absorption profile as described in the following subsection.

### 5.4.1 Fitting differential absorption with Voigt profiles

Our goal is to fit the observed differential absorption from the previous section. First, we characterize a single absorption feature as a Voigt profile function, considering physical processes that affect its shape as variables of the function. Second, we construct a Voigt profile ratio function, which will characterize the observed differential absorption.
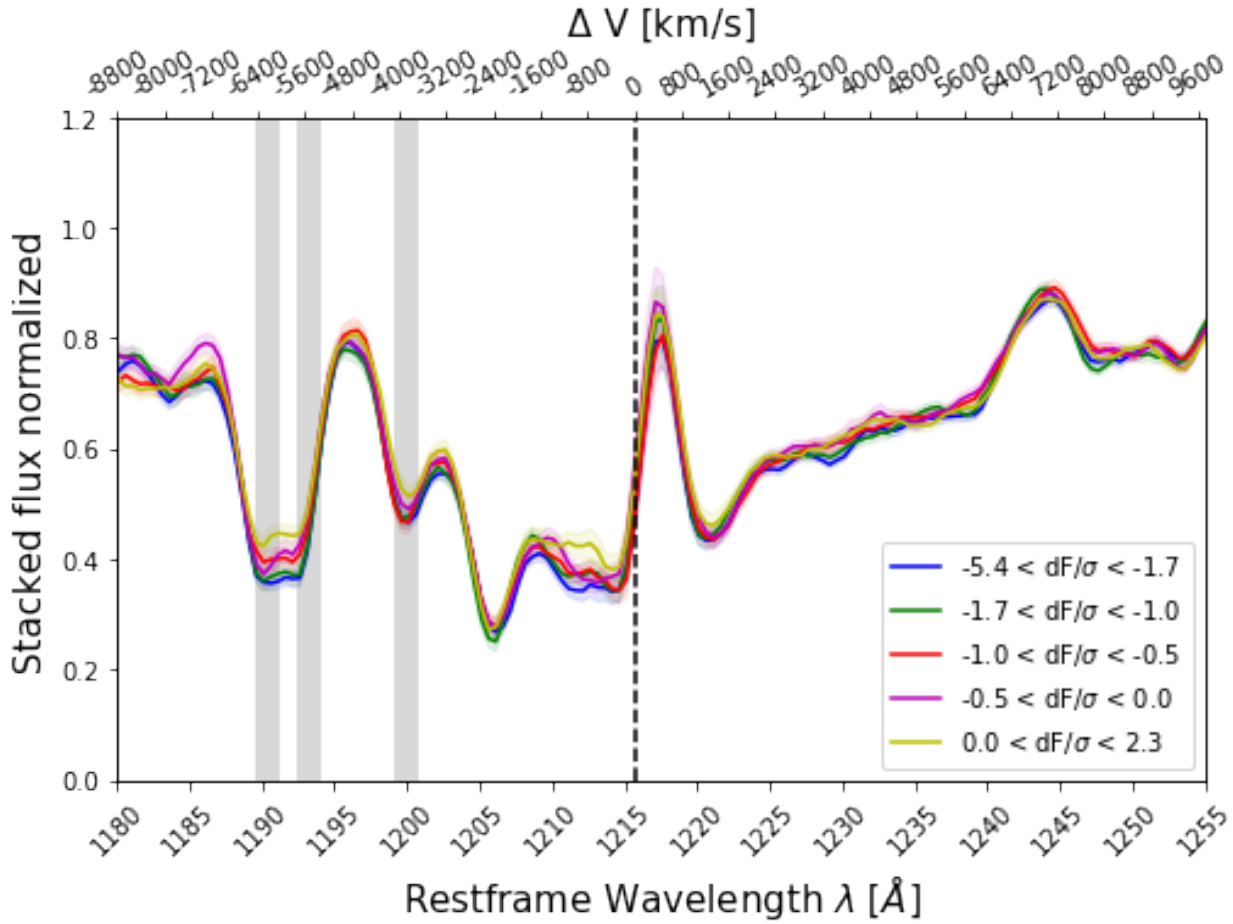
Figure 5.4: Stacked galaxy spectra of our sample divided into local density bins. x-axis present both rest frame wavelength and $\Delta V$, Ly$\alpha$ emission at 1215.67 is marked with dashed line. Grey vertical lines mark known metals in the spectra, the SII doublet and NI. Values of $\delta_f$ are normalized by $\sigma$
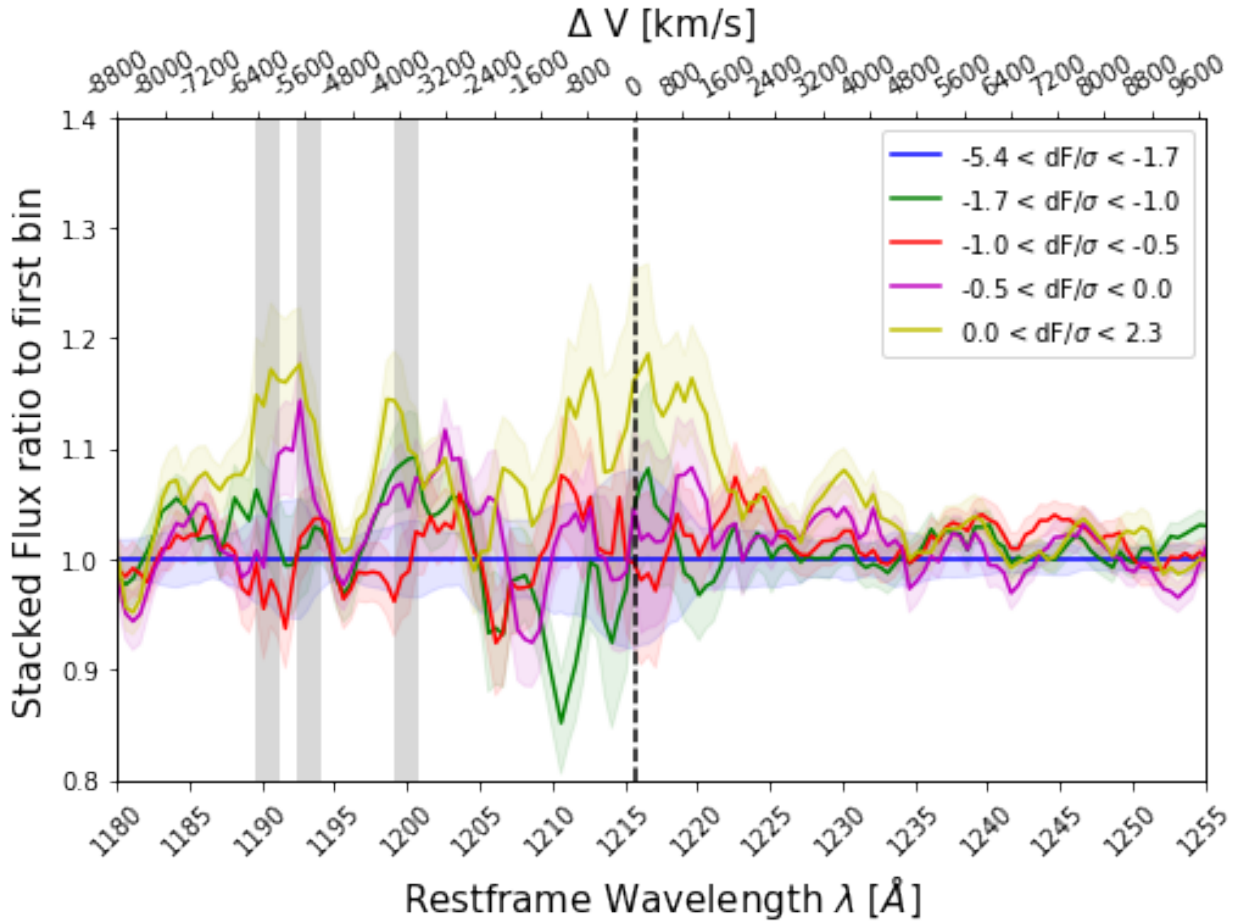
Figure 5.5: Stacked galaxy spectra by local density bins. Curves shows flux ratio between each density bin's spectrum and the spectrum of the first bin. Dashed vertical line marks Lyα emission restframe wavelength. Grey vertical lines mark known metals in the spectra: SII doublet and NI. A hint of some changes in differential absorption can be seen in the yellow curve, corresponding to galaxies in the lowest density environments. (See 5.4.1).

**Single Voigt profile function**

In order to fit absorption lines in galaxy spectra, it is necessary to take into account all the possible physical processes that affect their shape. Four parameters can be identified as the main ones: Column density (N), Doppler parameter (b), covering fraction (fcov) and velocity shift ($\Delta V$). The column density (N) affects the depth of the observed absorption. When it increases beyond the maximum depth (i.e., when flux reach 0), it starts showing dampening wings. As explained before in Section 5.3, these wings appear when column density reach very high values. The doppler parameter (b) is proportional to the gaussian width in velocity, and it affects the width of the observed absorption. The covering fraction (fcov) depends of the percentage of the galaxy that is covered with a certain column, scaling the absorption feature up or down. Finally $\Delta V$ models wavelenght redshift/blueshift of the restframe absorption feature in velocity units [km/s], shifting the absorption feature "to the left" or "to the right".

As noted in subsection 5.3 the observed absorption is extended over a broad range of velocity ($\sim 700$ km/s). Also, the width of the absorption profile gives us an indication of column density. Figure 5.5 shows a very wide differential absorption profile. This, and the fact that the feature is blueshifted, show us that probably this absorption corresponds to a damped absorption system as opposed to a low column density system.

Taking the previous physical explanation into account, a damped absorption profile is modeled using a Voigt profile function $V(N, f_{cov}, b, \Delta V)$ considering the following parameters:

- N: column density [cm$^{-2}$]
- $f_{cov}$: covering fraction
- b: Doppler parameter
- $\Delta V$: parameter to model wavelenght redshift/blueshift of the restframe absorption feature in velocity units [km/s]. Shift is transformed into wavelength ($\Delta\lambda$) and added up to the $\lambda$ value before evaluating the Voigt profile function.

The following equation describes said single Voigt profile:

$$V(\lambda, N, f_{cov}, \Delta V, b) = (1 - f_{cov}) + f_{cov} * e^{-\tau(\lambda + \Delta\lambda, N, b)} \tag{5.2}$$

Our data presents high column densities (N) meaning that damping wings dominate the profile, the resolution of our data (R=800) makes impossible to measure directly $b$ from the spectra where damping wing dominate, for that reason we fix the value of $b$ at 25 km/s inside the function. Also, the variable $\Delta V$ is fixed to $-300$ km/s as it is the typical velocity blueshift found in absorption Ly$alpha$ profiles (Reddy et al. 2016), so a shift in wavelenght equivalent to $-300$ km/s is applied to $\lambda$ inside the equation as a fixed value. With those changes applied, above equation simplifies into:

$$V(N, f_{cov}) = (1 - f_{cov}) + f_{cov} * e^{-\tau(N)} \tag{5.3}$$

Where the $\tau$ function is defined as:

$$\tau(N) = N * \sigma_0 * f_{osc} * H(\lambda)/(\sqrt{\pi} * \Delta\nu_D(b)) \tag{5.4}$$

Where N is the column density, $\sigma_0$ corresponds to the cross section, defined as $\sigma_0 = \frac{\pi e^2}{m_e c}$, with e = electron charge, $m_e$ = electron mass, and c = speed of light. Then $f_{osc}$ corresponds to Oscillator strength and its value is $f_{osc} = 0.4164$ according to Morton 2003. $\Delta\nu_D(b)$ is another function depending on b, defined as: $\Delta\nu_D(b) = \frac{b\nu_0}{c}$ ; where $\nu_0 = \frac{c}{121.567}$ [1/nm] is the Lyman alpha restframe frequency. Finally H is the Faddeeva function = H(x,y). It appears because the integral of the Voigt profile can be evaluated as this function. Their variables are: $x(\lambda) = \frac{\nu - \nu_0}{\Delta\nu_D}$ ; $\nu = \frac{c}{\lambda}$ ; $y = \frac{\gamma}{4\pi\Delta\nu_D}$ ; and $\gamma = 6.258 \times 10^8 \ s^{-1}$.

Equations 5.3 and 5.4 describe a single Voigt profile considering the four main physical parameters that affect the shape of the absorption features. As we described above, we choose to work with only two of the four variables (N, fcov), fixing the values of b and $\Delta V$.

**Ratio of two Voigt profiles function**
Since we are fitting a differential absorption, a function for the ratio of two single Voigt profiles is needed. We simply take the ratio of two single Voigt profiles, as can be seen in the following equation:

$$V_{ratio}(N1, fcov1, N2, fcov2) = \frac{V2(N2, fcov2)}{V1(N1, fcov1)} \tag{5.5}$$

$$V_{ratio}(N1, fcov1, N2, fcov2) = \frac{(1 - f_{cov2}) + f_{cov2} * e^{-\tau(N2)}}{(1 - f_{cov1}) + f_{cov1} * e^{-\tau(N1)}} \tag{5.6}$$

Some adjustments are made to the above function to fit the parameters in a more optimal way. First, from the inspection of Figure 5.5 we can conclude that the column density (N) is similar between the spectra in the ratio plots. If, for example, N1 was considerably different to N2 in any of the curves, we should see a bimodal residual in the ratio plots due the damping wings. Since bimodal residuals are not observed, we assume the same column density for both curves at the moment of fitting (N1 = N2 = N). Also, instead of fitting the covering fraction for each curve separately ($fcov1, fcov2$), we fit the ratio between the two curves as a single variable called $covratio$, which relates $fcov1$ and $fcov2$ through the following equation: $covratio = \frac{1 - fcov2}{1 - fcov1}$. $fcov1$ value is fixed at $fcov1 = 0.95$ following Reddy et al. 2016.

Applying the changes we reduce 4 parameters for fitting $(N1, fcov1, N2, fcov2)$ to only 2 (N, covratio), as shown in the following equation:

$$V_{ratio}(N, covratio) = \frac{(0.05 * covratio) + (1 - 0.05 * covratio) * e^{-\tau N}}{0.05 + 0.95 * e^{-\tau N}} \tag{5.7}$$

Where:

- N : Column density.

- *covratio*: Covering fraction ratio factor between stacked spectra.

Additionally, we calculate the errors for the fitted ratio flux with the following equation:

$$f_{error} = g^T * pcov * g \tag{5.8}$$

where *pcov* is the covariance matrix, the output by the `curve fit` function, considering spectra errors, and $g$ is a vector with the partial derivatives of the flux ratio against every fitted parameter. $g^T$ is the transposed $g$ vector.

$$g = [\frac{\partial F}{\partial N}, \frac{\partial F}{\partial covratio}, \frac{\partial F}{\partial \Delta V}] \tag{5.9}$$

At first, when inspecting the ratio curves, we expected to be able to fit the differential absorption without masking the flux of the Ly$\alpha$ emission line region. but some excess emission flux can still be seen in the ratio curves. Before fitting the ratio curves with the ratio Voigt profile function defined above, we mask the observed Ly$\alpha$ emission region ($0$ km/s $< \Delta_V <$ $800$ km/s), shown as a grey column in the Figures 5.6.

The fitted Voigt profile ratio with error bars for every ratio spectra are show in figure 5.6. Values obtained for both fitted parameters (N, covratio), and their errors ($\sigma_N$, $\sigma_{covratio}$) for each bin are shown in Table 5.1. In order to compare differential absorption between local density bins, $\frac{N}{\sigma_N}$ and $\frac{(1-covratio)}{\sigma_{covratio}}$ are reported as a measure of the significance of the differential absorption fitted parameters.

|  | N [cm$^{-2}$] | $\sigma_N$ | N / $\sigma_N$ | covratio | $\sigma_{covratio}$ | $\lvert 1 - covratio \rvert$ / $\sigma_{covratio}$ |
|---|---|---|---|---|---|---|
| (a) 1st vs 2nd bin | 1.94e+21 | 9.59e+20 | 2.02 | 1.101 | 0.044 | 2.29 |
| (b) 1st vs 3rd bin | 1.87e+21 | 1.54e+21 | 1.20 | 0.954 | 0.031 | 1.48 |
| (c) 1st vs 4th bin | 2.45e+21 | 3.16e+21 | 0.77 | 0.972 | 0.027 | 1.03 |
| (d) 1st vs 5th bin | 5.84e+21 | 1.54e+21 | 3.78 | 0.897 | 0.018 | 5.72 |

Table 5.1: Values of the 2 parameters and their 2 corresponding errors of *Voigt profile ratio* function fitted to each ratio stacked spectra. In order to compare differential absorption between local density bins, $\frac{N}{\sigma_N}$ and $(1 - covratio)/sigma_{covratio}$ are reported as a measure of the significance of the differential absorption.

Finally, from figure 5.6 and Table 5.1 there is a clear evidence of a trend of differential absorption through different bins of local density. Looking at the four panels of figure 5.6 the differential absorption starts as a negative curve for the highest local density bin (panel a), meaning that the studied bin presents higher Ly$\alpha$ absorption than the first one. The fitted parameters present a 2 $\sigma$ significance. For intermediate local densities (panels b and c), the value of fitted parameters (N and *covratio*) are undetermined (N / $\sigma_N \sim 1$, |1-covratio|/$\sigma_{covratio} \sim 1$). No statistically significant interpretation can be done for these intermediate local density bins. Finally panel (d), the group of lowest local density, shows a significant differential absorption. It can be seen from Table 5.1 that the significance of
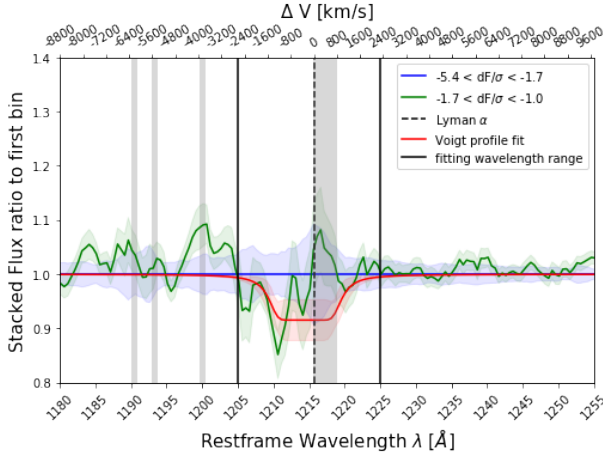
(a) First vs second group stacked flux ratio
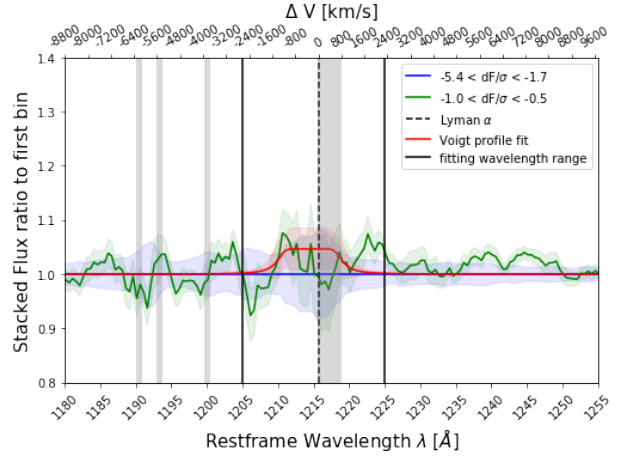
(b) First vs third group stacked flux ratio
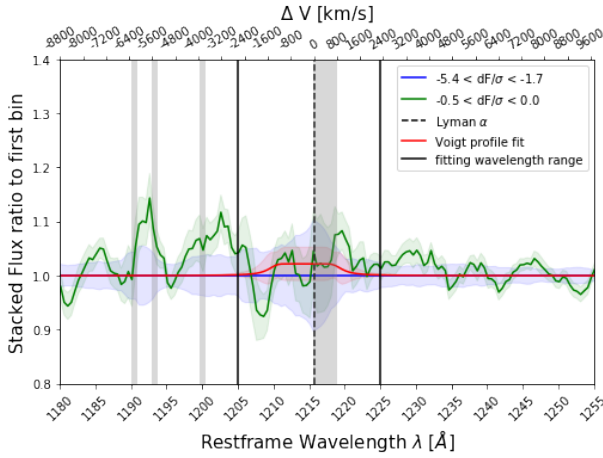
(c) First vs fourth group stacked flux ratio
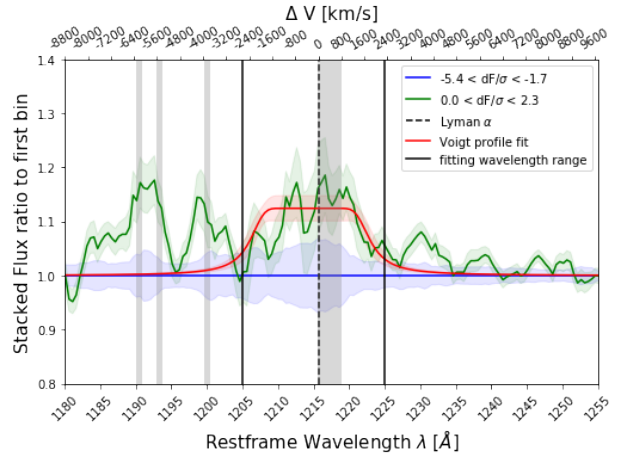
(d) First vs fifth group stacked flux ratio

Figure 5.6: Voigt profiles fitted to the ratio stacked spectra between the first bin of galaxies and the other 4 bins. First bin curve is used for normalization and its error is shown in blue. In each panel the corresponding stacked spectrum are shown in green. Fitted Voigt profiles ratios are shown in red. In the lower local density bin (the right bottom panel) a significant differential absorption feature is observed.

the parameters is very high, with 3 $\sigma$ for N and $\sim 5\sigma$ for *covratio*. Given these results we can confirm an observed trend for differential absorption as local density changes. Higher absorption are observed at higher local densities.

This study aims to report this observed trend but not to analyse the possible physical explanations behind it. This means that, even we see a trend over a local density range, it does not necessarily mean that the observed effect is produced by environmental conditions. This effect could arise from the fact that different galaxy populations live in different environments. In the case of these absorption studies, compared with the emission studies of Sections 3 and 4, we do not have a model to characterize the effects of galaxy properties over Ly$\alpha$ absorption. We can not characterize it and isolate the effects of environmental conditions over the absorption, as we did on emission studies.

Further studies with the LATIS complete sample could confirm this observed trend. And a proper modeling of the physics behind the Ly$\alpha$ absorption feature is needed to explain why is it found.

# Conclusion

In this thesis we present a study of the impact of large scale structure on the Ly$\alpha$ emission and absorption of high redshift galaxies (z $\sim 2.2 - 2.8$), using preliminary results of a new Ly$\alpha$ forest tomography survey called: Lyman Alpha Tomography IMACS Survey, LATIS (see Section 2.1). A. B. Newman et al. 2020 present it as a spectroscopic survey at Magellan (LCO), designed to map the $z = 2.2 - 2.8$ IGM in three dimensions by observing the Ly$\alpha$ forest in the spectra of galaxies and QSOs .

We perform separate Ly$\alpha$ emission and absorption studies using the $\sim 2900$ galaxy spectra of LBGs that compose the LATIS survey. We also use the environmental density ($\delta f$) derived in A. B. Newman et al. 2020 from the tomographic reconstruction of the LATIS survey spectra, to study how the Ly$\alpha$ emission and absorption properties of galaxies depend on environment.

In order to study the effect of environment on Ly$\alpha$ emission it is necessary to take into account how this emission is affected by the internal properties (e.g. luminosity, dust content) of the galaxies that populate different environments. Oyarzun et al. 2017's work determined how Ly$\alpha$ EW and escape probabilities depend on galaxy properties, creating a Probability of Equivalent Width distribution of Ly$\alpha$ model P(EW) depending on UV magnitude ($M_{UV}$) and UV slope ($\beta$).

In Section 3 we first obtain the $M_{UV}$ and $\beta$ from available CFHTLS photometry. We use it to estimate P(EW) with the model proposed by Oyarzun et al. 2017. We expect to estimate the baseline level of variation in the Ly$\alpha$ EW distribution between different environmental density bins in our sample, simply due to changes in galaxy internal properties. We obtain the probability of EW: P(EW) for each group. Then, we determine if there are any changes due to galaxy properties on each density bin. We find that there is not a significant trend/changes over P(EW) due to internal procesess over different environmental conditions. This allow us to interpret any change found in the following sections as an effect of environment and not due to internal galaxy properties.

In Section 4 we directly measure the EW for each galaxy in each density bin, following Kornei et al. 2010 method. After measuring EW, we study EW distributions through different local density bins and see how they change with local density. To do that, an exponential function is fitted to each EW distribution, and the fitted parameters changes are observed for each density bin. We find no statistically significant changes in the EW distribution of Ly$\alpha$ emission as a function of density for galaxies in the preliminary LATIS sample.

In Section 5 we search for variations in the Ly$\alpha$ absorption profile of galaxies as a function of environment. In a first exploration, we find a significant decrease in HI absorption around galaxies living the lowest density environments compared to the highest density ones. To characterize this found trend, we create stacked spectra for each studied density bin. We also create ratio curves comparing stacked curved with respect to the first density bin, as a representation of the differential absorption. We perform a differential Voigt profile ratio fitting over the ratio curves, and confirm the trend where higher density bins present more absorption that lower denisity environments. From the fitted parameters we interpret the reduced absorption as a lower covering fraction of HI gas.

This study aims to report this observed trend but not to analyse the possible physical explanations behind it. This means that, even we see a trend over a local density range, it does not necessarily mean that the observed effect is produced by environmental conditions. This effect could arise from the fact that different galaxy populations live in different environments. In the case of these absorption studies, compared with the emission studies of Sections 3 and 4, we do not have a model to characterize the effects of galaxy properties over Ly$\alpha$ absorption. We can not characterize it and isolate the effects of environmental conditions in the observed absorption, as we did on emission studies.

Further studies with the LATIS complete sample could confirm this observed trend. And a proper modeling of the physics behind the Ly$\alpha$ absorption feature is needed to explain why is it found.

# Bibliography

Adams, J. J., Blanc, G. A., Hill, G. J., Gebhardt, K., Drory, N., Hao, L., Bender, R., Byun, J., Ciardullo, R., Cornell, M. E., Finkelstein, S. L., Fry, A., Gawiser, E., Gronwall, C., Hopp, U., Jeong, D., Kelz, A., Kelzenberg, R., Komatsu, E., ... Wilkinson, C. P. (2011). The HETDEX Pilot Survey. I. Survey Design, Performance, and Catalog of Emission-line Galaxies. ApJS, *192*(1), arXiv 1011.0426, 5. https://doi.org/10.1088/0067-0049/192/1/5

Adelberger, K. L., Shapley, A. E., Steidel, C. C., Pettini, M., Erb, D. K., & Reddy, N. A. (2005). The Connection between Galaxies and Intergalactic Absorption Lines at Redshift 2$<_<$~3. ApJ, *629*(2), arXiv astro-ph/0505122, 636–653. https://doi.org/10.1086/431753

Adelberger, K. L., Steidel, C. C., Shapley, A. E., & Pettini, M. (2003). Galaxies and Intergalactic Matter at Redshift z~3: Overview. ApJ, *584*(1), arXiv astro-ph/0210314, 45–75. https://doi.org/10.1086/345660

Bamford, S. P., Nichol, R. C., Baldry, I. K., Land, K., Lintott, C. J., Schawinski, K., Slosar, A., Szalay, A. S., Thomas, D., Torki, M., Andreescu, D., Edmondson, E. M., Miller, C. J., Murray, P., Raddick, M. J., & Vandenberg, J. (2009). Galaxy Zoo: the dependence of morphology and colour on environment*. MNRAS, *393*(4), arXiv 0805.2612, 1324–1352. https://doi.org/10.1111/j.1365-2966.2008.14252.x

Blanc, G. A., Adams, J. J., Gebhardt, K., Hill, G. J., Drory, N., Hao, L., Bender, R., Ciardullo, R., Finkelstein, S. L., Fry, A. B., Gawiser, E., Gronwall, C., Hopp, U., Jeong, D., Kelzenberg, R., Komatsu, E., MacQueen, P., Murphy, J. D., Roth, M. M., ... Tufts, J. (2011). The HETDEX Pilot Survey. II. The Evolution of the Ly$\alpha$ Escape Fraction from the Ultraviolet Slope and Luminosity Function of $1.9 < z < 3.8$ LAEs. ApJ, *736*(1), arXiv 1011.0430, 31. https://doi.org/10.1088/0004-637X/736/1/31

Blanton, M. R., & Moustakas, J. (2009). Physical Properties and Environments of Nearby Galaxies. ARA&A, *47*(1), arXiv 0908.3017, 159–210. https://doi.org/10.1146/annurev-astro-082708-101734

Cantalupo, S., Arrigoni-Battaia, F., Prochaska, J. X., Hennawi, J. F., & Madau, P. (2014). A cosmic web filament revealed in Lyman-$\alpha$ emission around a luminous high-redshift quasar. Nature, *506*(7486), arXiv 1401.4469, 63–66. https://doi.org/10.1038/nature12898

Caucci, S., Colombi, S., Pichon, C., Rollinde, E., Petitjean, P., & Sousbie, T. (2008). Recovering the topology of the intergalactic medium at z ~2. MNRAS, *386*(1), 211–229. https://doi.org/10.1111/j.1365-2966.2008.13016.x

Chen, H.-W., Lanzetta, K. M., & Webb, J. K. (2001). The Origin of C IV Absorption Systems at Redshifts z < 1: Discovery of Extended C IV Envelopes around Galaxies. ApJ, *556*(1), arXiv astro-ph/0104403, 158–163. https://doi.org/10.1086/321537

Chiang, Y.-K., Overzier, R., & Gebhardt, K. (2013). Ancient Light from Young Cosmic Cities: Physical and Observational Signatures of Galaxy Proto-clusters. ApJ, *779*(2), arXiv 1310.2938, 127. https://doi.org/10.1088/0004-637X/779/2/127

Chonis, T. S., Blanc, G. A., Hill, G. J., Adams, J. J., Finkelstein, S. L., Gebhardt, K., Kollmeier, J. A., Ciardullo, R., Drory, N., Gronwall, C., Hagen, A., Overzier, R. A., Song, M., & Zeimann, G. R. (2013). The Spectrally Resolved Lyα Emission of Three Lyα-selected Field Galaxies at z ~2.4 from the HETDEX Pilot Survey. ApJ, *775*(2), arXiv 1308.1957, 99. https://doi.org/10.1088/0004-637X/775/2/99

Christensen, C. R., Davé, R., Governato, F., Pontzen, A., Brooks, A., Munshi, F., Quinn, T., & Wadsley, J. (2016). In-N-Out: The Gas Cycle from Dwarfs to Spiral Galaxies. ApJ, *824*(1), arXiv 1508.00007, 57. https://doi.org/10.3847/0004-637X/824/1/57

Cooke, J. [J.], Omori, Y., & Ryan-Weber, E. V. (2013). Nurturing Lyman break galaxies: observed link between environment and spectroscopic features. MNRAS, *433*(3), arXiv 1305.0562, 2122–2141. https://doi.org/10.1093/mnras/stt875

Cooke, J. [Jeff], Wolfe, A. M., Gawiser, E., & Prochaska, J. X. (2006). Survey for Galaxies Associated with z ~3 Damped Lyα Systems. II. Galaxy-Absorber Correlation Functions. ApJ, *652*(2), arXiv astro-ph/0607149, 994–1010. https://doi.org/10.1086/507476

Cooper, M. C., Newman, J. A., Croton, D. J., Weiner, B. J., Willmer, C. N. A., Gerke, B. F., Madgwick, D. S., Faber, S. M., Davis, M., Coil, A. L., Finkbeiner, D. P., Guhathakurta, P., & Koo, D. C. (2006). The DEEP2 Galaxy Redshift Survey: the relationship between galaxy properties and environment at z ~1. MNRAS, *370*(1), arXiv astro-ph/0603177, 198–212. https://doi.org/10.1111/j.1365-2966.2006.10485.x

Crighton, N. H. M., Bielby, R., Shanks, T., Infante, L., Bornancini, C. G., Bouché, N., Lambas, D. G., Lowenthal, J. D., Minniti, D., Morris, S. L., Padilla, N., Péroux, C., Petitjean, P., Theuns, T., Tummuangpak, P., Weilbacher, P. M., Wisotzki, L., & Worseck, G. (2011). The VLT LBG Redshift Survey- II. Interactions between galaxies and the IGM at z∼ 3. MNRAS, *414*(1), arXiv 1006.4385, 28–49. https://doi.org/10.1111/j.1365-2966.2011.17247.x

Darvish, B., Mobasher, B., Martin, D. C., Sobral, D., Scoville, N., Stroe, A., Hemmati, S., & Kartaltepe, J. (2017). Cosmic Web of Galaxies in the COSMOS Field: Public Catalog and Different Quenching for Centrals and Satellites. ApJ, *837*(1), arXiv 1611.05451, 16. https://doi.org/10.3847/1538-4357/837/1/16

Darvish, B., Mobasher, B., Sobral, D., Rettura, A., Scoville, N., Faisst, A., & Capak, P. (2016). The Effects of the Local Environment and Stellar Mass on Galaxy Quenching to z ∼ 3. ApJ, *825*(2), arXiv 1605.03182, 113. https://doi.org/10.3847/0004-637X/825/2/113

Dressler, A. [A.]. (1980). Galaxy morphology in rich clusters: implications for the formation and evolution of galaxies. ApJ, *236*, 351–365. https://doi.org/10.1086/157753

Dressler, A. [Alan], Bigelow, B., Hare, T., Sutin, B., Thompson, I., Burley, G., Epps, H., Oemler, J., Augustus, Bagish, A., Birk, C., Clardy, K., Gunnels, S., Kelson, D., Shectman, S., & Osip, D. (2011). IMACS: The Inamori-Magellan Areal Camera and Spectrograph on Magellan-Baade. PASP, *123*(901), 288. https://doi.org/10.1086/658908

Dressler, A. [Alan], Oemler, J., Augustus, Couch, W. J., Smail, I., Ellis, R. S., Barger, A., Butcher, H., Poggianti, B. M., & Sharples, R. M. (1997). Evolution since z = 0.5 of

the Morphology-Density Relation for Clusters of Galaxies. ApJ, *490*(2), arXiv astro-ph/9707232, 577–591. https://doi.org/10.1086/304890

Faucher-Giguère, C.-A., Kereš, D., & Ma, C.-P. (2011). The baryonic assembly of dark matter haloes. MNRAS, *417*(4), arXiv 1103.0001, 2982–2999. https://doi.org/10.1111/j.1365-2966.2011.19457.x

Faucher-Giguère, C.-A., Prochaska, J. X., Lidz, A., Hernquist, L., & Zaldarriaga, M. (2008). A Direct Precision Measurement of the Intergalactic Ly$\alpha$ Opacity at $2 <= z <= 4.2$. ApJ, *681*(2), arXiv 0709.2382, 831–855. https://doi.org/10.1086/588648

Ford, A. B., Davé, R., Oppenheimer, B. D., Katz, N., Kollmeier, J. A., Thompson, R., & Weinberg, D. H. (2014). Tracing inflows and outflows with absorption lines in circumgalactic gas. MNRAS, *444*(2), arXiv 1309.5951, 1260–1281. https://doi.org/10.1093/mnras/stu1418

Gallerani, S., Kitaura, F. S., & Ferrara, A. (2011). Cosmic density field reconstruction from Ly$\alpha$ forest data. MNRAS, *413*(1), arXiv 1011.6228, L6–L10. https://doi.org/10.1111/j.1745-3933.2011.01020.x

Gnedin, N. Y., & Hui, L. (1998). Probing the Universe with the Lyalpha forest - I. Hydrodynamics of the low-density intergalactic medium. MNRAS, *296*(1), arXiv astro-ph/9706219, 44–55. https://doi.org/10.1046/j.1365-8711.1998.01249.x

Gronke, M., Dijkstra, M., McCourt, M., & Oh, S. P. (2016). From Mirrors to Windows: Lyman-alpha Radiative Transfer in a Very Clumpy Medium. ApJ, *833*(2), arXiv 1611.01161, L26. https://doi.org/10.3847/2041-8213/833/2/L26

Gronke, M., Dijkstra, M., McCourt, M., & Oh, S. P. (2017). Resonant line transfer in a fog: using Lyman-alpha to probe tiny structures in atomic gas. A&A, *607*arXiv 1704.06278, A71. https://doi.org/10.1051/0004-6361/201731013

Hagen, A., Ciardullo, R., Gronwall, C., Acquaviva, V., Bridge, J., Zeimann, G. R., Blanc, G. A., Bond, N. A., Finkelstein, S. L., Song, M., Gawiser, E., Fox, D. B., Gebhardt, H., Malz, A. I., Schneider, D. P., Drory, N., Gebhardt, K., & Hill, G. J. (2014). Spectral Energy Distribution Fitting of HETDEX Pilot Survey Ly$\alpha$ Emitters in COSMOS and GOODS-N. ApJ, *786*(1), arXiv 1403.4935, 59. https://doi.org/10.1088/0004-637X/786/1/59

Hahn, C., Blanton, M. R., Moustakas, J., Coil, A. L., Cool, R. J., Eisenstein, D. J., Skibba, R. A., Wong, K. C., & Zhu, G. (2015). PRIMUS: Effects of Galaxy Environment on the Quiescent Fraction Evolution at $z < 0.8$. ApJ, *806*(2), arXiv 1412.7162, 162. https://doi.org/10.1088/0004-637X/806/2/162

Hayes, M., Schaerer, D., Östlin, G., Mas-Hesse, J. M., Atek, H., & Kunth, D. (2011). On the Redshift Evolution of the Ly$\alpha$ Escape Fraction and the Dust Content of Galaxies. ApJ, *730*(1), arXiv 1010.4796, 8. https://doi.org/10.1088/0004-637X/730/1/8

Heckman, T. M., Borthakur, S., Overzier, R., Kauffmann, G., Basu-Zych, A., Leitherer, C., Sembach, K., Martin, D. C., Rich, R. M., Schiminovich, D., & Seibert, M. (2011). Extreme Feedback and the Epoch of Reionization: Clues in the Local Universe. ApJ, *730*(1), arXiv 1101.4219, 5. https://doi.org/10.1088/0004-637X/730/1/5

Hennawi, J. F., Prochaska, J. X., Cantalupo, S., & Arrigoni-Battaia, F. (2015). Quasar quartet embedded in giant nebula reveals rare massive structure in distant universe. *Science*, *348*(6236), arXiv 1505.03786, 779–783. https://doi.org/10.1126/science.aaa5397

Hill, G. J., Gebhardt, K., Komatsu, E., Drory, N., MacQueen, P. J., Adams, J., Blanc, G. A., Koehler, R., Rafal, M., Roth, M. M., Kelz, A., Gronwall, C., Ciardullo, R.,

& Schneider, D. P. (2008). The Hobby-Eberly Telescope Dark Energy Experiment (HETDEX): Description and Early Pilot Survey Results (T. Kodama, T. Yamada, & K. Aoki, Eds.). In T. Kodama, T. Yamada, & K. Aoki (Eds.), *Panoramic views of galaxy formation and evolution*.

Hill, G. J., & HETDEX Consortium. (2016). HETDEX and VIRUS: Panoramic Integral Field Spectroscopy with 35k Fibers (I. Skillen, M. Balcells, & S. Trager, Eds.). In I. Skillen, M. Balcells, & S. Trager (Eds.), *Multi-object spectroscopy in the next decade: Big questions, large surveys, and wide fields*.

Horowitz, B., Lee, K.-G., White, M., Krolewski, A., & Ata, M. (2019). TARDIS. I. A Constrained Reconstruction Approach to Modeling the z $\sim$ 2.5 Cosmic Web Probed by Ly$\alpha$ Forest Tomography. ApJ, *887*(1), arXiv 1903.09049, 61. https://doi.org/10.3847/1538-4357/ab4d4c

Ilbert, O., Capak, P., Salvato, M., Aussel, H., McCracken, H. J., Sanders, D. B., Scoville, N., Kartaltepe, J., Arnouts, S., Le Floc'h, E., Mobasher, B., Taniguchi, Y., Lamareille, F., Leauthaud, A., Sasaki, S., Thompson, D., Zamojski, M., Zamorani, G., Bardelli, S., ... Zucca, E. (2009). Cosmos Photometric Redshifts with 30-Bands for 2-deg$^2$. ApJ, *690*(2), arXiv 0809.2101, 1236–1249. https://doi.org/10.1088/0004-637X/690/2/1236

Kakiichi, K., & Dijkstra, M. (2018). A new model framework for circumgalactic Ly $\alpha$ radiative transfer constrained by galaxy-Ly $\alpha$ forest clustering. MNRAS, *480*(4), arXiv 1710.10053, 5140–5159. https://doi.org/10.1093/mnras/sty2214

Kakiichi, K., Majumdar, S., Mellema, G., Ciardi, B., Dixon, K. L., Iliev, I. T., Jelić, V., Koopmans, L. V. E., Zaroubi, S., & Busch, P. (2017). Recovering the H II region size statistics from 21-cm tomography. MNRAS, *471*(2), arXiv 1702.02520, 1936–1954. https://doi.org/10.1093/mnras/stx1568

Kauffmann, G., White, S. D. M., Heckman, T. M., Ménard, B., Brinchmann, J., Charlot, S., Tremonti, C., & Brinkmann, J. (2004). The environmental dependence of the relations between stellar mass, structure, star formation and nuclear activity in galaxies. MNRAS, *353*(3), arXiv astro-ph/0402030, 713–731. https://doi.org/10.1111/j.1365-2966.2004.08117.x

Kollmeier, J. A., Weinberg, D. H., Davé, R., & Katz, N. (2003). Lyman Break Galaxies and the Ly$\alpha$ Forest. ApJ, *594*(1), arXiv astro-ph/0209563, 75–96. https://doi.org/10.1086/376789

Kornei, K. A., Shapley, A. E., Erb, D. K., Steidel, C. C., Reddy, N. A., Pettini, M., & Bogosavljević, M. (2010). The Relationship between Stellar Populations and Ly$\alpha$ Emission in Lyman Break Galaxies. ApJ, *711*(2), arXiv 0911.2000, 693–710. https://doi.org/10.1088/0004-637X/711/2/693

Krolewski, A., Lee, K.-G., White, M., Hennawi, J. F., Schlegel, D. J., Nugent, P. E., Lukić, Z., Stark, C. W., Koekemoer, A. M., Le Fèvre, O., Lemaux, B. C., Maier, C., Rich, R. M., Salvato, M., & Tasca, L. (2018). Detection of z $\sim$ 2.3 Cosmic Voids from 3D Ly$\alpha$ Forest Tomography in the COSMOS Field. ApJ, *861*(1), arXiv 1710.02612, 60. https://doi.org/10.3847/1538-4357/aac829

Kulkarni, V. P., Ellison, S. L., Lopez, S., & Som, D. (2015). Probing Structure in Cold Gas at z < 1 with Gravitationally Lensed Quasar Sightlines.

Lee, K.-G., Hennawi, J. F., White, M., Prochaska, J. X., Font-Ribera, A., Schlegel, D. J., Rich, R. M., Suzuki, N., Stark, C. W., Le Fèvre, O., Nugent, P. E., Salvato, M., & Zamorani, G. (2016). Shadow of a Colossus: A z = 2.44 Galaxy Protocluster Detected

in 3D Lyα Forest Tomographic Mapping of the COSMOS Field. ApJ, *817*(2), arXiv 1509.02833, 160. https://doi.org/10.3847/0004-637X/817/2/160

Lee, K.-G., Hennawi, J., Stark, C., Prochaska, J. X., White, M., Schlegel, D. J., Eilers, A.-C., Arinyo-i-Prats, A., Suzuki, N., Croft, R. A. C., Caputi, K. I., Cassata, P., Ilbert, O., Garilli, B., Koekemoer, A. M., Le Brun, V., Le Fevre, O., Maccagni, D., Nugent, P., . . . Zucca, E. (2014). Lyα Forest Tomography from Background Galaxies: The First Megaparsec-resolution Large-scale Structure Map at z > 2. ApJ, *795*(1), arXiv 1409.5632, L12. https://doi.org/10.1088/2041-8205/795/1/L12

Lee, K.-G., Krolewski, A., White, M., Schlegel, D., Nugent, P. E., Hennawi, J. F., Müller, T., Pan, R., Prochaska, J. X., Font-Ribera, A., Suzuki, N., Glazebrook, K., Kacprzak, G. G., Kartaltepe, J. S., Koekemoer, A. M., Le Fèvre, O., Lemaux, B. C., Maier, C., Nanayakkara, T., . . . Tran, K.-V. H. (2018). First Data Release of the COSMOS Lyα Mapping and Tomography Observations: 3D Lyα Forest Tomography at 2.05 < z < 2.55. ApJS, *237*(2), arXiv 1710.02894, 31. https://doi.org/10.3847/1538-4365/aace58

Lemaux, B. C. (2019). The Nature of Nurture: An Optical/NIR Exploration of High-Density Environments at z>2, In *Aas/high energy astrophysics division*.

Madau, P., Weisz, D. R., & Conroy, C. (2014). Reversal of Fortune: Increased Star Formation Efficiencies in the Early Histories of Dwarf Galaxies? ApJ, *790*(2), arXiv 1406.0838, L17. https://doi.org/10.1088/2041-8205/790/2/L17

McDonald, P., Miralda-Escudé, J., & Cen, R. (2002). Large-Scale Correlation of Mass and Galaxies with the Lyα Forest Transmitted Flux. ApJ, *580*(1), arXiv astro-ph/0112476, 42–53. https://doi.org/10.1086/343031

McQuinn, M. (2016). The Evolution of the Intergalactic Medium. ARA&A, *54* arXiv 1512.00086, 313–362. https://doi.org/10.1146/annurev-astro-082214-122355

Momose, R., Ouchi, M., Nakajima, K., Ono, Y., Shibuya, T., Shimasaku, K., Yuma, S., Mori, M., & Umemura, M. (2014). Diffuse Lyα haloes around galaxies at z = 2.2-6.6: implications for galaxy formation and cosmic reionization. MNRAS, *442*(1), arXiv 1403.0732, 110–120. https://doi.org/10.1093/mnras/stu825

Morton, D. C. (2003). Atomic Data for Resonance Absorption Lines. III. Wavelengths Longward of the Lyman Limit for the Elements Hydrogen to Gallium. ApJS, *149*(1), 205–238. https://doi.org/10.1086/377639

Murdin, P. (2000). *Encyclopedia of Astronomy and Astrophysics*.

Muzzin, A., Wilson, G., Yee, H. K. C., Gilbank, D., Hoekstra, H., Demarco, R., Balogh, M., van Dokkum, P., Franx, M., Ellingson, E., Hicks, A., Nantais, J., Noble, A., Lacy, M., Lidman, C., Rettura, A., Surace, J., & Webb, T. (2012). The Gemini Cluster Astrophysics Spectroscopic Survey (GCLASS): The Role of Environment and Self-regulation in Galaxy Evolution at z ~1. ApJ, *746*(2), arXiv 1112.3655, 188. https://doi.org/10.1088/0004-637X/746/2/188

Newman, A. B., Rudie, G. C., Blanc, G. A., Kelson, D. D., Rhoades, S., Hare, T., Pérez, V., Benson, A. J., Dressler, A., Gonzalez, V., Kollmeier, J. A., Konidaris, N. P., Mulchaey, J. S., Rauch, M., Le Fèvre, O., Lemaux, B. C., Cucciati, O., & Lilly, S. J. (2020). LATIS: The Lyα Tomography IMACS Survey. ApJ, *891*(2), arXiv 2002.10676, 147. https://doi.org/10.3847/1538-4357/ab75ee

Newman, A., Bezanson, R., Johnson, S., Rudie, G., Greene, J., Hummels, C., Bundy, K., Giavalisco, M., Kartaltepe, J., Kriek, M., Law, D., Lemoine-Busserolle, M., Malkan, M., Marchesini, D., Nelson, E., Pierce, M., Ravindranath, S., Strom, A., Tran, K.-V.,

& Whitaker, K. (2019). Resolving Galaxy Formation at Cosmic Noon. BAAS, *51*(3), 145.

Oppenheimer, B. D., Davé, R., Kereš, D., Fardal, M., Katz, N., Kollmeier, J. A., & Weinberg, D. H. (2010). Feedback and recycled wind accretion: assembling the z = 0 galaxy mass function. MNRAS, *406*(4), arXiv 0912.0519, 2325–2338. https://doi.org/10.1111/j.1365-2966.2010.16872.x

Ouchi, M., Harikane, Y., Shibuya, T., Shimasaku, K., Taniguchi, Y., Konno, A., Kobayashi, M., Kajisawa, M., Nagao, T., Ono, Y., Inoue, A. K., Umemura, M., Mori, M., Hasegawa, K., Higuchi, R., Komiyama, Y., Matsuda, Y., Nakajima, K., Saito, T., & Wang, S.-Y. (2018). Systematic Identification of LAEs for Visible Exploration and Reionization Research Using Subaru HSC (SILVERRUSH). I. Program strategy and clustering properties of ˜2000 Ly$\alpha$ emitters at z = 6-7 over the 0.3-0.5 Gpc$^2$ survey area. PASJ, *70*arXiv 1704.07455, S13. https://doi.org/10.1093/pasj/psx074

Overzier, R. A. (2016). The realm of the galaxy protoclusters. A review. A&A Rev., *24*(1), arXiv 1610.05201, 14. https://doi.org/10.1007/s00159-016-0100-3

Oyarzun, G., Blanc, G., Gonzalez, V., Mateo, M., & Bailey, I., John I. (2017). A Comprehensive Study of Ly$\alpha$ Emission in the High-redshift Galaxy Population. ApJ, *843*(2), arXiv 1706.01886, 133. https://doi.org/10.3847/1538-4357/aa7552

Oyarzun, G., Blanc, G., Gonzalez, V., Mateo, M., Bailey, I., John I., Finkelstein, S. L., Lira, P., Crane, J. D., & Olszewski, E. W. (2016). How Lyman Alpha Emission Depends on Galaxy Stellar Mass. ApJ, *821*(1), arXiv 1604.03113, L14. https://doi.org/10.3847/2041-8205/821/1/L14

Patel, S., Kelson, D. D., Holden, B. P., Illingworth, G. D., Franx, M., van der Wel, A., & Ford, H. (2009). A Wide-field Study of the z 0.8 Cluster RX J0152.7-1357: The Role of Environment in Galaxy Evolution, In *American astronomical society meeting abstracts #213*.

Pelliccia, D., Lemaux, B. C., Tomczak, A. R., Lubin, L. M., Shen, L., Epinat, B., Wu, P.-F., Gal, R. R., Rumbaugh, N., Kocevski, D. D., Tresse, L., & Squires, G. (2019). Searching for environmental effects on galaxy kinematics in groups and clusters at z ˜ 1 from the ORELSE survey. MNRAS, *482*(3), arXiv 1807.04763, 3514–3549. https://doi.org/10.1093/mnras/sty2876

Peng, Y.-j., Lilly, S. J., Kovač, K., Bolzonella, M., Pozzetti, L., Renzini, A., Zamorani, G., Ilbert, O., Knobel, C., Iovino, A., Maier, C., Cucciati, O., Tasca, L., Carollo, C. M., Silverman, J., Kampczyk, P., de Ravel, L., Sanders, D., Scoville, N., . . . Scaramella, R. (2010). Mass and Environment as Drivers of Galaxy Evolution in SDSS and zCOSMOS and the Origin of the Schechter Function. ApJ, *721*(1), arXiv 1003.4747, 193–221. https://doi.org/10.1088/0004-637X/721/1/193

Pichon, C., Vergely, J. L., Rollinde, E., Colombi, S., & Petitjean, P. (2001). Inversion of the Lyman $\alpha$ forest: three-dimensional investigation of the intergalactic medium. MNRAS, *326*(2), arXiv astro-ph/0105196, 597–620. https://doi.org/10.1046/j.1365-8711.2001.04595.x

Postman, M., & Geller, M. J. (1984). The morphology-density relation - The group connection. ApJ, *281*, 95–99. https://doi.org/10.1086/162078

Rakic, O., Schaye, J., Steidel, C. C., & Rudie, G. C. (2012). Neutral Hydrogen Optical Depth near Star-forming Galaxies at z ≈ 2.4 in the Keck Baryonic Structure Survey. ApJ, *751*(2), arXiv 1109.4944, 94. https://doi.org/10.1088/0004-637X/751/2/94

Rauch, M. (1998). The Lyman Alpha Forest in the Spectra of QSOs. ARA&A, *36* arXiv astro-ph/9806286, 267–316. https://doi.org/10.1146/annurev.astro.36.1.267

Reddy, N. A., Steidel, C. C., Pettini, M., Bogosavljević, M., & Shapley, A. E. (2016). The Connection Between Reddening, Gas Covering Fraction, and the Escape of Ionizing Radiation at High Redshift. ApJ, *828*(2), arXiv 1606.03452, 108. https://doi.org/10.3847/0004-637X/828/2/108

Rudie, G. C., Steidel, C. C., Pettini, M., Trainor, R. F., Strom, A. L., Hummels, C. B., Reddy, N. A., & Shapley, A. E. (2019). Column Density, Kinematics, and Thermal State of Metal-bearing Gas within the Virial Radius of z ∼ 2 Star-forming Galaxies in the Keck Baryonic Structure Survey. ApJ, *885*(1), arXiv 1903.00004, 61. https://doi.org/10.3847/1538-4357/ab4255

Rudie, G. C., Steidel, C. C., Trainor, R. F., Rakic, O., Bogosavljević, M., Pettini, M., Reddy, N., Shapley, A. E., Erb, D. K., & Law, D. R. (2012). The Gaseous Environment of High-z Galaxies: Precision Measurements of Neutral Hydrogen in the Circumgalactic Medium of z ~2-3 Galaxies in the Keck Baryonic Structure Survey. ApJ, *750*(1), arXiv 1202.6055, 67. https://doi.org/10.1088/0004-637X/750/1/67

Shapley, A. E., Steidel, C. C., Pettini, M., & Adelberger, K. L. (2003). Rest-Frame Ultraviolet Spectra of z~3 Lyman Break Galaxies. ApJ, *588*(1), arXiv astro-ph/0301230, 65–89. https://doi.org/10.1086/373922

Stark, C. W., White, M., Lee, K.-G., & Hennawi, J. F. (2015). Protocluster discovery in tomographic Ly $\alpha$ forest flux maps. MNRAS, *453*(1), arXiv 1412.1507, 311–327. https://doi.org/10.1093/mnras/stv1620

Stark, D. P., Ellis, R. S., Chiu, K., Ouchi, M., & Bunker, A. (2010). Keck spectroscopy of faint 3 < z < 7 Lyman break galaxies - I. New constraints on cosmic reionization from the luminosity and redshift-dependent fraction of Lyman $\alpha$ emission. MNRAS, *408*(3), arXiv 1003.5244, 1628–1648. https://doi.org/10.1111/j.1365-2966.2010.17227.x

Steidel, C. C., Bogosavljević, M., Shapley, A. E., Kollmeier, J. A., Reddy, N. A., Erb, D. K., & Pettini, M. (2011). Diffuse Ly$\alpha$ Emitting Halos: A Generic Property of High-redshift Star-forming Galaxies. ApJ, *736*(2), arXiv 1101.2204, 160. https://doi.org/10.1088/0004-637X/736/2/160

Steidel, C. C., Erb, D. K., Shapley, A. E., Pettini, M., Reddy, N., Bogosavljević, M., Rudie, G. C., & Rakic, O. (2010). The Structure and Kinematics of the Circumgalactic Medium from Far-ultraviolet Spectra of z ~= 2-3 Galaxies. ApJ, *717*(1), arXiv 1003.0679, 289–322. https://doi.org/10.1088/0004-637X/717/1/289

Steidel, C., Martin, C., Prochaska, J. X., Pettini, M., Schaye, J., & Rakic, O. (2009). Mapping the 'Cosmic Web' During the Peak Epoch of Galaxy Formation, In *Astro2010: The astronomy and astrophysics decadal survey.*

Theuns, T., & Srianand, R. (2006). ELT requirements for future observations of the Intergalactic Medium (P. Whitelock, M. Dennefeld, & B. Leibundgut, Eds.). In P. Whitelock, M. Dennefeld, & B. Leibundgut (Eds.), *The scientific requirements for extremely large telescopes.* https://doi.org/10.1017/S1743921306001141

Treu, T., Schmidt, K. B., Trenti, M., Bradley, L. D., & Stiavelli, M. (2013). The Changing Ly$\alpha$ Optical Depth in the Range 6 < z < 9 from the MOSFIRE Spectroscopy of Y-dropouts. ApJ, *775*(1), arXiv 1308.5985, L29. https://doi.org/10.1088/2041-8205/775/1/L29

Tripp, T. M., & Song, L. (2012). The 21 cm "Outer Arm" and the Outer-galaxy High-velocity Clouds: Connected by Kinematics, Metallicity, and Distance. ApJ, *746*(2), arXiv 1101.1107, 173. https://doi.org/10.1088/0004-637X/746/2/173

Tumlinson, J., Thom, C., Werk, J. K., Prochaska, J. X., Tripp, T. M., Weinberg, D. H., Peeples, M. S., O'Meara, J. M., Oppenheimer, B. D., Meiring, J. D., Katz, N. S., Davé, R., Ford, A. B., & Sembach, K. R. (2011). The Large, Oxygen-Rich Halos of Star-Forming Galaxies Are a Major Reservoir of Galactic Metals. *Science*, *334*(6058), arXiv 1111.3980, 948. https://doi.org/10.1126/science.1209840

Tummuangpak, P., Bielby, R. M., Shanks, T., Theuns, T., Crighton, N. H. M., Francke, H., & Infante, L. (2014). The Very Large Telescope Lyman-Break Galaxy Redshift Survey - IV. Gas and galaxies at z ∼ 3 in observations and simulations. MNRAS, *442*(3), arXiv 1304.4598, 2094–2115. https://doi.org/10.1093/mnras/stu828

Turner, M. L., Schaye, J., Steidel, C. C., Rudie, G. C., & Strom, A. L. (2014). Metal-line absorption around z ≈ 2.4 star-forming galaxies in the Keck Baryonic Structure Survey. MNRAS, *445*(1), arXiv 1403.0942, 794–822. https://doi.org/10.1093/mnras/stu1801

van Dokkum, P., Brammer, G., Momcheva, I., Skelton, R. E., & Whitaker, K. E. (2013). 3D-HST Data Release v3.0: Extremely Deep Spectra in the UDF and WFC3 Mosaics in the 3D-HST/CANDELS Fields. *arXiv e-prints*, arXiv 1305.2140, arXiv:1305.2140.

Werk, J. K., Prochaska, J. X., Tumlinson, J., Peeples, M. S., Tripp, T. M., Fox, A. J., Lehner, N., Thom, C., O'Meara, J. M., Ford, A. B., Bordoloi, R., Katz, N., Tejos, N., Oppenheimer, B. D., Davé, R., & Weinberg, D. H. (2014). The COS-Halos Survey: Physical Conditions and Baryonic Mass in the Low-redshift Circumgalactic Medium. ApJ, *792*(1), arXiv 1403.0947, 8. https://doi.org/10.1088/0004-637X/792/1/8

Zheng, Z., Cen, R., Trac, H., & Miralda-Escudé, J. (2010). Radiative Transfer Modeling of Lyα Emitters. I. Statistics of Spectra and Luminosity. ApJ, *716*(1), arXiv 0910.2712, 574–598. https://doi.org/10.1088/0004-637X/716/1/574

Zheng, Z., Cen, R., Trac, H., & Miralda-Escudé, J. (2011). Radiative Transfer Modeling of Lyα Emitters. II. New Effects on Galaxy Clustering. ApJ, *726*(1), arXiv 1003.4990, 38. https://doi.org/10.1088/0004-637X/726/1/38